

2023-10-23

# First-order phase transitions in Yang-Mills theories and the density of state method

Lucini, B

<https://pearl.plymouth.ac.uk/handle/10026.1/22180>

---

10.1103/physrevd.108.074517

Physical Review D

American Physical Society (APS)

---

*All content in PEARL is protected by copyright law. Author manuscripts are made available in accordance with publisher policies. Please cite only the published version using the details provided on the item record or document. In the absence of an open licence (e.g. Creative Commons), permissions for further reuse of content should be sought from the publisher or author.*

# First-order phase transitions in Yang-Mills theories and the density of state method

Biagio Lucini<sup>\*</sup>

*Department of Mathematics, Faculty of Science and Engineering, Swansea University,  
Fabian Way, Swansea SA1 8EN, Wales, United Kingdom  
and Swansea Academy of Advanced Computing, Swansea University,  
Fabian Way, Swansea SA1 8EN, Wales, United Kingdom*

David Mason<sup>†</sup>

*Department of Physics, Faculty of Science and Engineering, Swansea University,  
Singleton Park, Swansea SA2 8PP, Wales, United Kingdom  
and Department of Mathematics, Faculty of Science and Engineering, Swansea University,  
Fabian Way, Swansea SA1 8EN, Wales, United Kingdom*

Maurizio Piai<sup>‡</sup>

*Department of Physics, Faculty of Science and Engineering, Swansea University,  
Singleton Park, Swansea SA2 8PP, Wales, United Kingdom*

Enrico Rinaldi<sup>§</sup>

*Interdisciplinary Theoretical and Mathematical Science Program, RIKEN (iTHEMS),  
2-1 Hirosawa, Wako, Saitama 351-0198, Japan*

Davide VDACCHINO<sup>||</sup>

*School of Mathematics and Hamilton Mathematics Institute, Trinity College, Dublin 2, Ireland  
and Centre for Mathematical Sciences, University of Plymouth, Plymouth PL4 8AA, United Kingdom*



(Received 14 July 2023; accepted 20 September 2023; published 23 October 2023)

When studied at finite temperature, Yang-Mills theories in  $3 + 1$  dimensions display the presence of confinement/deconfinement phase transitions, which are known to be of first order—the  $SU(2)$  gauge theory being the exception. Theoretical as well as phenomenological considerations indicate that it is essential to establish a precise characterization of these physical systems in proximity of such phase transitions. We present and test a new method to study the critical region of parameter space in non-Abelian quantum field theories on the lattice, based upon the logarithmic linear relaxation (LLR) algorithm. We apply this method to the  $SU(3)$  Yang-Mills lattice gauge theory, and perform extensive calculations with one fixed choice of lattice size. We identify the critical temperature, and measure interesting physical quantities near the transition. Among them, we determine the free energy of the model in the critical region, exposing for the first time its multivalued nature with a numerical calculation from first principles, providing this novel evidence in support of a first-order phase transition. This study sets the stage for future high-precision measurements, by demonstrating the potential of the method.

DOI: [10.1103/PhysRevD.108.074517](https://doi.org/10.1103/PhysRevD.108.074517)

<sup>\*</sup>b.lucini@swansea.ac.uk

<sup>†</sup>2036508@Swansea.ac.uk

<sup>‡</sup>m.piai@swansea.ac.uk

<sup>§</sup>erinaldi.work@gmail.com

<sup>||</sup>davide.vadacchino@plymouth.ac.uk

*Published by the American Physical Society under the terms of the [Creative Commons Attribution 4.0 International](https://creativecommons.org/licenses/by/4.0/) license. Further distribution of this work must maintain attribution to the author(s) and the published article's title, journal citation, and DOI. Funded by SCOAP<sup>3</sup>.*

## I. INTRODUCTION

The characterization of phase transitions is a central topic of study in theoretical physics, both for reasons of principle and in view of applications. In the proximity of second-order phase transitions, for critical values of the control parameters, the correlation length diverges, hence such systems can be classified in universality classes, distinguished by the value of quantities that are independent of the microscopic details. But this is atypical, while many important physical systems undergo first-order phase

transitions, which admit no notion of universality. It is then essential to specify the details of the theory, and identify computational strategies optimized to the precise determination of model-dependent physical observables. The latent heat is a particularly important example, as it determines the strength of the transition.

A case in point, within fundamental physics, is provided by the history of electroweak baryogenesis. One of the three conditions identified by Sakharov [1] to explain the matter-antimatter asymmetry in the observable Universe requires the dynamics to be out of equilibrium. Hence, the electroweak phase transition should be of first order and strong enough, if it is to play a central role in these phenomena. Testing this hypothesis required developing a program of dedicated calculations. The final outcome of this challenging endeavor is that electroweak baryogenesis cannot work within the standard model (SM) of particle physics; it was demonstrated nonperturbatively [2–8] that a line of first-order phase transitions ends at a critical point, and that the transition disappears into a crossover, except for unrealistically light Higgs boson masses,  $m_h < \mathcal{O}(70)$  GeV. This result still stands nowadays as prominent evidence for new physics. (See Refs. [9,10] for reviews, and also Ref. [11] for a recent nonperturbative update.)

New physics is also needed to explain the origin of dark matter, the existence of which is supported by both observational astrophysics and cosmology. This evidence motivates proposals postulating the existence of hidden sectors, comprised of (dark) particles carrying no SM quantum numbers, feebly coupled to SM particles (see, e.g., Refs. [12–18]). Hidden sector dark matter scenarios find concrete realizations as composite dark matter (as, for example, in Refs. [19–28]) and strongly interacting dark matter (see, e.g., Refs. [29–36]). Loosely inspired by quantum chromodynamics (QCD), their microscopic description consists of new confining gauge theories, with or without matter field content.

If the new dark sector undergoes a first-order phase transition in the early Universe, it would yield a relic stochastic background of gravitational waves [37–42], potentially accessible to a number of present and future gravitational wave experiments [43–60]. Model-independent studies of the properties of such cosmological confinement phase transitions and their imprint on the stochastic gravitation background may adopt either of two complementary theoretical strategies for investigation. (See, e.g., Fig. 1 of Ref. [61] but also Refs. [62–65].) Either one models the bubble nucleation rates by using the results of direct nonperturbative calculation of latent heat, surface tension and other relevant dynamical quantities; or one builds and constrains an effective description, such as the Polyakov-loop model [61,63,66–74], or matrix models [62,75–83], supplementing it by thermodynamic information computed, again, nonperturbatively.

Either way, one arrives at a characterization of the phase transition in terms of a set of parameters; critical temperature,  $T_c$ , percolation temperature,  $T_*$ , strength of the transition,  $\alpha$ , inverse duration of the transition,  $\beta/H_*$ , bubble wall velocity,  $v_w$ , and number of degrees of freedom after the transition,  $g_*$ . These are then used as input in the cosmological evolution, via existing software packages such as, for example, PTPlot [59], to obtain the power spectrum of relic stochastic gravitational waves,  $h^2\Omega_{\text{GW}}$ , that can be compared with detector reach.

Hence, the first step towards calculating the power spectrum of gravitational waves requires precise nonperturbative treatment of the dynamics, which can be provided by numerical simulations of lattice gauge theories. The finite-temperature behavior of many lattice gauge theories has been studied in the past; for example, for  $SU(N_c)$  see Refs. [84–89], for  $Sp(N_c)$  see Ref. [90], and for  $G_2$  see Ref. [91–94]. These pioneering works were somewhat limited in scope, while dedicated high-precision measurements of specific observables, in particular of the latent heat, present technical challenges. A handful of dedicated lattice calculations has started to appear, focused on stealth dark matter with  $SU(4)$  gauge dynamics [95–97], or on  $Sp(4)$  gauge theories [98–100]. A complementary approach to the study of the relevant out-of-equilibrium dynamics near criticality, bubble nucleation, and bubble wall velocity makes use of the nonperturbative tools provided by gauge-gravity dualities [101–104], which can be generalized to strongly coupled systems exhibiting confinement and chiral symmetry breaking [105–114]—we refer the reader to Refs. [115–122] and references therein for interesting examples along these lines.

The history of the studies of  $SU(3)$  gauge theories is quite interesting as a general illustration of how the field has been evolving. The recent Ref. [123] critically summarizes this history, discusses the technical difficulties intrinsic to current state-of-the-art lattice calculations, and addresses some of the challenges with the extrapolation to the continuum limit in proximity of the phase transition. Among the salient points in such history, is the fact that the pure gauge theory undergoes a first-order phase transition, which has been accepted for a while [124,125]. Finite-temperature lattice studies of the theory coupled to heavy quarks have given encouraging results [126–131] but are still ongoing. More generally, considerable activity is taking part in QCD, see Ref. [132] for a recent summary. The thermodynamics of pure  $SU(3)$  Yang-Mills theories has been studied intensively [133–145], and we know that the phase transition is not strong, hence difficult to characterize.

Our interest in the characterization of the confinement/deconfinement phase transition originates in the ongoing research program on  $Sp(N_c)$  lattice gauge theories [146–155] and their composite bound states. Our long-term aim is to measure observable quantities, such as the latent heat at the transition, which have potential implications for dark matter

and for stochastic gravitational-wave detection. We approach this goal by exploiting a recent proposal, which is based upon the density of states and provides an alternative to Monte Carlo importance sampling (IS) methods; the logarithmic linear relaxation (LLR) algorithm [156–159]. We describe the method in the body of the paper. It is worth mentioning that the literature on finite-temperature studies of  $Sp(N_c)$  gauge theories is rather limited [90], as is the application of the LLR algorithm: Abelian gauge theories have been studied in detail [158], while in the non-Abelian case the properties of  $SU(3)$  have been investigated at zero temperature [159], and preliminary finite-temperature results exist for  $SU(4)$  [160,161] and  $SU(N_c)$  [162].

We hence take a conservative approach. In this paper, we apply the LLR algorithm to the best understood  $SU(3)$  Yang-Mills theory. We study the theory with one representative lattice, to set benchmarks for the future large-scale task of performing infinite volume and continuum limit extrapolations. We confirm the presence of a metastability compatible with the established first-order phase transition arising in the system, determine the corresponding pseudocritical temperature using known definitions, and measure the discontinuity that leads to the latent heat. Our results are consistent with other approaches, and we can achieve the desired precision level. In parallel, we started also to explore  $Sp(N_c)$  Yang-Mills theories, in particular  $Sp(4)$ , about which we will report in a separate publication.

The paper is organized as follows. We describe the LLR algorithm and its relation to the density of state in Sec. II. This section builds upon the method introduced in Ref. [158], and serves the purpose of setting the notation and making the exposition self-contained. Section III summarizes the basic properties of the lattice theory of interest, and the definitions of the relevant observables. The main body of the paper consists of Secs. IV and V. This work sets the stage for our future investigations, discussed briefly in Sec. VI. We relegate to Appendices A–C technical details about the algorithm we use, and the tests we performed to validate it. Some partial, preliminary results of the research project we report upon in this paper have been presented in contributions to conference proceedings [163,164], but here we present updated results, including a comprehensive and self-contained discussion of the procedure we follow and an extended set of observables.

## II. DENSITY OF STATES

We start by defining the density of states, a quantity that plays a central role in our calculations, and discussing its numerical determination. The path integral of a quantum field theory (QFT), with degrees of freedom expressed by the field(s)  $\phi$  and Euclidean action  $S[\phi]$ , can be written as

$$Z(\beta) \equiv \int [D\phi] e^{-\beta S[\phi]}, \quad (1)$$

where the coupling  $\beta$  (not to be confused with  $\beta/H_*$ ) has been exposed. The density of states,  $\rho(E)$ , is the measure of the hypersurface in field-configuration space spanned by the fields when the constraint  $S = E$  is imposed,

$$\rho(E) \equiv \int [D\phi] \delta(S[\phi] - E). \quad (2)$$

Using the density of states, the path integral of the theory can be rewritten as

$$Z(\beta) = \int dE \rho(E) e^{-\beta E}. \quad (3)$$

This expression of the path integral is particularly convenient for observables,  $O(E)$ , that only depend on the action, since their expectation value can be reformulated as a one-dimensional integral,

$$\langle O \rangle_\beta = \frac{\int dE \rho(E) O(E) e^{-\beta E}}{\int dE \rho(E) e^{-\beta E}}. \quad (4)$$

Hence, knowing the density of states provides a route to the computation of these observables. In addition, as we show later in this section, using the density of states, one can also access observables that have a more general dependency on the fields, not expressible in terms of the action alone.

The density of states can be computed efficiently by using the linear logarithmic relaxation method [156,158,159,165]. The algorithm exposed in this work is based on a variation of the LLR algorithm with the replica exchange method introduced in Ref. [165], the key difference being that in this work we are going to replace the two nonoverlapping half-shifted replica sequences with a single sequence of half-overlapping consecutive subintervals. The algorithm depends on a set of tunable parameters, which we introduce and describe in this section. For reference, these parameters are summarized in Table I.

As a first step, we divide an interval of interest,  $E_{\min} \leq E \leq E_{\max}$ , into  $2N - 1$  overlapping subintervals of fixed width,  $\Delta_E = (E_{\max} - E_{\min})/N$ , where each of the subintervals but the first and the last have an overlap of amplitude  $\Delta_E/2$  with the preceeding and the following subinterval. As we shall see below, the overlap can be exploited to ensure the ergodicity of the algorithm. The subintervals are numbered with an index,  $n$ , ranging from  $n = 1$  (corresponding to central action value  $E_{\min} + \Delta_E/2$ ) to  $2N - 1$  (central action  $E_{\max} - \Delta_E/2$ ). In each subinterval  $1 \leq n \leq 2N - 1$ , the central action is  $E_n = E_{\min} + n\Delta_E/2$ . We approximate the density of states,  $\rho(E)$ , with the piecewise linear function  $\log \tilde{\rho}(E) \sim \log \rho(E)$ , defined as

$$\log \tilde{\rho}(E) \equiv a_n(E - E_n) + c_n, \quad (5)$$

TABLE I. Parameters of the LLR algorithm used for the numerical computation of the density of states as formulated in this work for  $(2N - 1)$  overlapping subintervals, each of amplitude  $\Delta_E$ , covering the relevant action interval,  $[E_{\min}, E_{\max}]$ .

Symbol	Name/Role	Description/Purpose
$E_{\min}$	Minimal action	Lower limit of the relevant action interval
$E_{\max}$	Maximal action	Upper limit of the relevant action interval
$\Delta_E$	Amplitude of subintervals	Controls the local first-order expansion of $\log \rho(E)$
$\bar{m}$	Number of NR steps	Enables to refine the initial guess for the $a_n$
$\tilde{m}$	Number of RM updates	Controls the tolerance on the convergence of the $a_n$
$n_{Th}$	Number of thermalization steps per RM update	Controls decorrelation between two RM updates
$n_M$	Number of measurements per RM update	Controls the accuracy of the expectation values in Eq. (14)
$n_P$	Number of action-constrained updates per RM update	$n_{Th} + n_M$
$n_S$	Number of RM updates between swaps	Ensures ergodicity of the algorithm
$n_R$	Number of determinations of the $a_n$	Enables to estimate statistical errors

where  $E_n - \Delta_E/4 \leq E \leq E_n + \Delta_E/4$ , for each  $n$ . This choice provides a prescription to deal unambiguously with the overlapping regions in the subinterval, assigning each half of the overlap to the subinterval with the nearest central action. The purpose of the LLR algorithm is to calculate numerically the  $a_n$  and  $c_n$  coefficients, assuming continuity of the function  $\log \tilde{\rho}(E)$  in the interval  $[E_{\min}, E_{\max}]$ .

As a second step, given any observable,  $O(E)$ , we define  $2N - 1$  restricted expectation values,  $\langle\langle O \rangle\rangle_n$ , as follows:

$$\langle\langle O \rangle\rangle_n(a) \equiv \frac{1}{\mathcal{N}_n(a)} \int_{E_n - \frac{\Delta_E}{2}}^{E_n + \frac{\Delta_E}{2}} O(E) \rho(E) e^{-aE} dE, \quad (6)$$

where the normalization factor is given by

$$\mathcal{N}_n(a) \equiv \int_{E_n - \frac{\Delta_E}{2}}^{E_n + \frac{\Delta_E}{2}} \rho(E) e^{-aE} dE. \quad (7)$$

One now sees that if  $a = a_n$  of Eq. (5), then the exponential factor inside the integrals in these definitions is  $e^{-a_n E} = e^{-a_n E_n + c_n} / \tilde{\rho}$ , and the constant factor,  $e^{-a_n E_n + c_n}$ , cancels between numerator and denominator, so that the weight factor in the integrals in Eqs. (6) and (7) is just  $\rho(E) / \tilde{\rho}(E)$ . The main idea behind the algorithm is that we consider  $\tilde{\rho}(E)$  to be a good approximation of  $\rho(E)$  if such weight factor,  $\rho(E) / \tilde{\rho}(E)$ , for the restricted expectation value in the

interval  $[E_n - \Delta_E/2, E_n + \Delta_E/2]$ , is approximately unit. More generally, we are interested in expectation values, where we need this factor to be constant (we will deal with the subinterval-dependent normalization constant below). Hence, we determine the value of  $a_n$  iteratively, by imposing the condition,

$$\begin{aligned} \langle\langle \Delta E \rangle\rangle_n(a_n) &= \frac{1}{\mathcal{N}_n(a_n)} \int_{E_n - \frac{\Delta_E}{2}}^{E_n + \frac{\Delta_E}{2}} (E - E_n) \rho(E) e^{-a_n E} dE \\ &= 0, \end{aligned} \quad (8)$$

for each  $n$ . The resulting stochastic equation makes use of the highly nontrivial information encoded in  $\rho(E)$ . As long as  $\Delta_E$  is sufficiently small, by Taylor expanding  $\log \rho(E)$  around  $E_n$  in Eq. (8), one sees that

$$a_n = \left. \frac{d \log \rho(E)}{dE} \right|_{E=E_n}. \quad (9)$$

For the third step, we adopt a combination of Newton-Raphson (NR) and Robbins-Monro (RM) algorithms [166] to solve iteratively Eq. (8). In a first sequence of iterations, we start from an initial trial value  $a_n^{(0)}$  and recursively update it, using the relation

$$a_n^{(m+1)} = a_n^{(m)} - \frac{\langle\langle \Delta E \rangle\rangle_n(a_n^{(m)})}{\langle\langle (\Delta E)^2 \rangle\rangle_n(a_n^{(m)})} \quad (10)$$

$$= a_n^{(m)} - \frac{\langle (E - E_n) [\theta(E - E_n + \frac{\Delta_E}{2}) - \theta(E - E_n - \frac{\Delta_E}{2})] \rangle_{a_n^{(m)}}}{\langle (E - E_n)^2 [\theta(E - E_n + \frac{\Delta_E}{2}) - \theta(E - E_n - \frac{\Delta_E}{2})] \rangle_{a_n^{(m)}}} \quad (11)$$

$$\simeq a_n^{(m)} - \frac{12}{\Delta_E^2} \left\langle (E - E_n) \left[ \theta \left( E - E_n + \frac{\Delta_E}{2} \right) - \theta \left( E - E_n - \frac{\Delta_E}{2} \right) \right] \right\rangle_{a_n^{(m)}}. \quad (12)$$



The above relation finds the root using one NR iteration. In the last step, the approximation consists of assuming the validity of a second-order expansion for the density of states in the action interval we are considering, which has been used to express the denominator of the correction term in closed form. The purpose of the initial NR iterations is to set up a convenient starting point for the more refined RM algorithm. This proves to be convenient, especially when

$$a_n^{(m+1)} = a_n^{(m)} - \frac{\alpha}{m+1} \frac{\langle\langle \Delta E \rangle\rangle_n(a_n^{(m)})}{\langle\langle (\Delta E)^2 \rangle\rangle_n(a_n^{(m)})} \quad (13)$$

$$\simeq a_n^{(m)} - \frac{\alpha}{m+1} \left( \frac{12}{\Delta_E^2} \right) \left\langle (E - E_n) \left[ \theta \left( E - E_n + \frac{\Delta_E}{2} \right) - \theta \left( E - E_n - \frac{\Delta_E}{2} \right) \right] \right\rangle_{a_n^{(m)}}. \quad (14)$$

This defines the RM step, which differs from the NR one by the damping factor  $\alpha/(m+1)$  of the calculated correction term. While not a strict requirement of the algorithm, for convenience we fix the positive constant to  $\alpha = 1$ . Again, Eq. (14) is obtained using a quadratic approximation of the density of states for a closed-form computation of  $\langle\langle (\Delta E)^2 \rangle\rangle_n(a_n^{(m)})$ , which assumes that the action interval is sufficiently small for the approximation to be sufficiently accurate. While the validity of this approximation is not crucial in the NR steps, since they are only used to refine the initialization, it is more important to verify its accuracy for the RM steps, since the latter determine the values of the  $a_n$  used in the calculation of the observables. The check is performed by verifying that with the obtained values of the  $a_n$  the action is uniformly distributed in the subinterval  $n$  (i.e., its histogram is flat within a predetermined tolerance), with the dynamics being compatible with a random walk. Since  $\Delta_E$  is a parameter of the calculation, it is always possible to restrict the subinterval width so that the quadratic approximation holds.

The right-hand sides of Eqs. (12) and (14) are evaluated by computing ordinary ensemble averages through importance sampling methods, in which the action is restricted to a small interval, and the weight redefined according to Eq. (6). The restriction can be done by rejecting update proposals that lead the action outside the subinterval of interest or—as we will do in this work—imposing constraints in the update proposals, so that each new trial value for the field variables to be updated, automatically respects the subinterval constraint (see Appendix A for further details). The recursion converges to  $a_n$  in the limit  $m \rightarrow \infty$ . We truncate the recursion at step  $\bar{m}$  and repeat the process from the start ensuring different random evolutions for  $a_n^{(m)}$ , changing the initialization of the random number sequences used in the process of generating the restricted averages. This yields a Gaussian-distributed set of final values  $a_n^{(\bar{m})}$ ,

insufficient prior knowledge is available on  $a_n$ . In these cases, even with rough initializations, for suitable choices of  $\bar{m}$ ,  $\bar{m}$  steps of the NR algorithm allows us to approach a value  $a_n^{(\bar{m})} \sim a_n$ , in proximity of the true value of  $a_n$ . We then refine the process, by defining a new trial initial value  $a_n^{(0)} \equiv a_n^{(\bar{m})}$  and recursively updating it using the modified relationship

with average  $a_n$  and standard deviation proportional to  $1/\sqrt{\bar{m}}$ , hence trading a truncation systematics with an error that can be treated statistically.

Restricting the averages to subintervals leads to ergodicity problems. To ensure ergodicity, we use the fact that at any given RM step the values of the actions in neighboring intervals have a finite probability of being in the overlapping region. When that happens, we can propose a Metropolis step that swaps the configurations in the two subintervals,

$$P_{\text{swap}} = \min(1, e^{(a_n^{(m)} - a_{n-1}^{(m)})(E_n^{(m)} - E_{n-1}^{(m)})}). \quad (15)$$

For these swap moves to be possible, simulations in the subintervals need to run in parallel, with the synchronization implemented by a controller process. This can be easily implemented with standard libraries such as the Message Passing Interface (MPI). However, even with this prescription, residual ergodicity problems can derive from the fact that  $E_{\min}$  and  $E_{\max}$  would otherwise be hard-action cutoffs. The resulting lack of ergodicity is prevented by extending the action range outside the  $[E_{\min}, E_{\max}]$  interval with two truncated Gaussians, one peaked at  $E_{\min} + \Delta_E/2$  and truncated at  $E_{\min} + \Delta_E$ , providing a prescription for dealing with  $E < E_{\min}$ , and the other peaked at  $E_{\max} - \Delta_E/2$  and truncated at  $E_{\max} - \Delta_E$  accounting for moves covering  $E > E_{\max}$ . Ergodicity is recovered by choosing those truncated Gaussians to coincide with the Boltzmann factors associated with  $\beta_{\text{upper}}$  and  $\beta_{\text{lower}}$ —the values of  $\beta$  at which the average actions correspond to  $E_{\min} + \Delta_E/2$  and to  $E_{\max} - \Delta_E/2$ . Appendix B describes how this is achieved in practice.

In our implementation, we propose a swap move between all neighbor intervals having energies in the overlapping regions after a fixed number,  $n_S$ , of RM updates. Each RM update consists of  $n_P = n_{Th} + n_M$

action-constrained updates. The  $n_{Th}$  updates decorrelate the configurations between RM updates, then  $n_M$  configurations are used for the calculation of expectation values in equation Eq. (14). This sequence of steps is repeated until we have performed  $\tilde{m}$  RM updates. As discussed previously, this process leads to a determination of the  $a_n$  for all values of  $n$ . Repeating it with different random number sequences, we get Gaussian distributed values of  $a_n$ , which can be used in a bootstrap analysis to provide a determination of the statistical uncertainty on observables.

Having determined the values of interest for  $a_n$ , continuity of  $\tilde{\rho}(E)$  at the boundaries of the subintervals requires

$$c_n = c_1 + \frac{\Delta_E}{4} a_1 + \frac{\Delta_E}{2} \sum_{k=2}^{n-1} a_k + \frac{\Delta_E}{4} a_n, \quad (16)$$

for all values of  $n > 1$ , and with the summation taking effect only when the upper index is bigger or equal to the lower one, i.e. for  $n \geq 3$ . This conditions leaves the value of  $c_1$  as a free parameter.  $c_1$  can be fixed by imposing a known global normalization condition. For instance, for  $\beta = \infty$ , the density of states must be equal to the number of degenerate vacua of the system. Nevertheless, in applications where the knowledge of the value of the path integral *per se* is not interesting, as is the case of observables expressed as ensemble averages, the normalization of the density of states can be fixed arbitrarily. In these cases, for simplicity, we choose  $c_1 = 0$ .

Having discussed the rationale for the various components of the method, for convenience, we now provide a summary of the algorithm:

- (i) Divide the interval  $[E_{\min}, E_{\max}]$  in  $2N - 1$  half-overlapping subintervals of amplitude  $\Delta_E$ , centered at energies  $E_1 = E_{\min} + \Delta_E/2, \dots, E_n = E_{\min} + n\Delta_E/2, \dots, E_{2N-1} = E_{\max} - \Delta_E/2$ . Define two half-Gaussians for prescribing rules for accepting/rejecting moves outside the interval  $[E_{\min}, E_{\max}]$ , with the correct Boltzmann distribution.
- (ii) Repeat  $n_R$  times with different random sequences:
  - (1) Initialize the values of  $a_n$ .
  - (2) Perform  $\tilde{m}$  steps of the NR algorithm, Eq. (11).
  - (3) Repeat  $\tilde{m}$  times:
    - (a) Perform  $n_P$  action-constrained updates (see Appendix A).
    - (b) Update  $a_n$  according to the RM prescription, Eq. (14).
    - (c) Repeat (a) and (b)  $n_S$  times.
    - (d) Propose a configuration swap according to Eq. (15).

Note that the swap step implies that the determination of  $a_n$  happens in parallel in the calculation, and requires a synchronization of the parallel processes. The parameters used in the algorithm are referenced in Table I. This algorithm provides  $n_R$  statistically independent determinations of  $a_n$ ,

and, consequently, of  $c_n$ , up to a prescription for fixing  $c_1$ , as described earlier in this section.

As shown in Ref. [158], the use of the LLR algorithm introduces a  $\Delta_E$ -dependent systematic error. Therefore, finite volume estimates of the quantities above can only be obtained after an extrapolation towards  $\Delta_E = 0$  has been performed. We devote Appendix C to a discussion of this process, for the lattice parameters adopted in this study.

We conclude by observing that the LLR method enables us to compute also canonical ensemble averages at coupling  $\beta$  of observables  $B[\phi]$  that have a dependency on the field  $\phi$  not leading to an explicit dependency on the action, using the formula [158],

$$\langle B[\phi] \rangle_\beta = \frac{1}{Z(\beta)} \sum_{n=1}^{2N-1} \frac{\Delta_E}{2} \tilde{\rho}(E_n) \tilde{B}[\phi], \quad (17)$$

where

$$\tilde{B}[\phi] = \langle \langle B[\phi] \exp(-\beta S[\phi] + a_n(S[\phi] - E_n)) \rangle \rangle_n(a_n). \quad (18)$$

### III. LATTICE SYSTEM

We compute ensemble averages with the distribution in the partition function of Eq. (1), by discretizing the degrees of freedom on a lattice. We focus on the action,  $S$ , of a four-dimensional Yang-Mills theory with non-Abelian gauge group  $SU(N_c)$  in Euclidean space, discretized as

$$S = \sum_p \left( 1 - \frac{1}{N_c} \text{ReTr}(U_p) \right), \quad (19)$$

which enters Eq. (1) with bare lattice coupling constant  $\beta = \frac{2N_c}{g_0^2}$ , related to the bare gauge coupling  $g_0^2$ . The summation runs over all the elementary plaquette variables,  $U_p$ , on the four-dimensional grid. Sampling of the link variables,  $U$ , representing the discretized gauge potential, entering the construction of the plaquette, are discussed in Appendix A. The measure is the product of integrals over the links.

We use hypercubic lattices with  $\tilde{V}/a^4 = N_T \times N_L^3$  points and isotropic lattice spacing  $a$ , in both temporal and spatial directions. We adopt periodic boundary conditions for the link variables in all directions. The thermodynamic temperature of the  $SU(N_c)$  Yang-Mills theory is  $T = \frac{1}{aN_T}$ . The lattice spacing,  $a$ , is dynamically controlled by the coupling,  $\beta$ , through the nonperturbative beta function of the theory, hence knowing  $\beta$  we can determine the temperature,  $T$ .

The order parameter for confinement is the Polyakov loop,  $l_p$ , defined as

$$l_p \equiv \frac{1}{N_c N_L^3} \sum_{\vec{x}} \text{Tr} \prod_{k=0}^{N_T-1} U_0(k\hat{0}, \vec{x}), \quad (20)$$

with  $\hat{0}$  the unit vector in the time direction. For  $T < T_c$ , the system lies in its confined phase,  $\langle l_p \rangle_\beta = 0$ . For  $T > T_c$  it lies in its deconfined phase,  $\langle l_p \rangle_\beta \in \mathbb{Z}_{N_c}$ , and the  $\mathbb{Z}_{N_c}$  symmetry of the action, Eq. (19), is spontaneously broken.

As the phase transition is of first order, it is characterized by a discontinuity in the first derivative of the free energy with respect to the temperature  $T$ , for  $T = T_c$ , that is recast in terms of the internal energy (density), defined as

$$\varepsilon(T) \equiv \frac{\kappa T^2}{V} \frac{\partial \ln Z(T)}{\partial T}, \quad (21)$$

where  $\kappa$  is the Boltzmann constant, which we set to  $\kappa = 1$ , and  $V = N_L^3 a^3$  is the spatial volume. At the phase transition, two distinct equilibrium states exist, with energies equal to  $\varepsilon_+$  and  $\varepsilon_-$ . The magnitude of the discontinuity across the transition,  $L_h \equiv |\varepsilon_+ - \varepsilon_-|$ , is known as *latent heat*. At exactly  $T = T_c$ , the system exhibits macroscopic configurations characterized by the presence of separating surfaces, on either side of which the order parameter has different values, and hysteresis can be observed in the evolution of the system. The configurations on either side of the transition have equal free energy, hence the rate of tunnelling is the same in either direction, giving rise to phase coexistence.

Yet, even when  $T \simeq T_c$  the physical system can still tunnel between the confined and deconfined phases, as the finiteness of the lattice system allows for metastable states to be physically realized in portions of the space, though they have finite lifetime. These phenomena present standard lattice algorithms with intrinsic difficulties, as the finiteness of the system implies that ensemble averages have nontrivial contaminations from metastable states, which ultimately smoothen the aforementioned nonanalyticity characterizing the transition. For example one still finds that the susceptibility of the Polyakov loop,

$$\chi_l(\beta) \equiv \langle |l_p|^2 \rangle_\beta - \langle |l_p| \rangle_\beta^2, \quad (22)$$

is expected to be maximal at  $T = T_c$ , though finite, and establishing the existence of a first-order phase transition requires nontrivial studies of the finite-volume scaling of  $\chi_l$ . As we will see, the LLR algorithm removes this difficulty, as it allows to access individually the physically stable and unstable states in configuration space, hence removing the practical problems due to tunneling and their effects on ensemble averaging.

Our aim is to characterize the phase transition in the  $SU(3)$  Yang-Mills theory, and ultimately determine the quantities  $T_c$  and  $L_h$ , extrapolated to infinite volume and to the continuum limit. In the body of this paper, we take a

first step in this direction, by studying a fixed lattice with  $N_T = 4$  and  $N_L = 20$ .

#### IV. METHODOLOGY

In this section, we provide precise relations between the values of the two main observables, critical temperature,  $T_c$ , and latent heat,  $L_h$ , and the density of states,  $\rho(E)$ , or, rather, its numerical estimate  $\tilde{\rho}(E)$ .

When studying a lattice theory by Monte Carlo sampling, a typical signal of tunneling between vacua is the presence of hops in the simulation-time evolution of the value of the action per plaquette,  $u_p$ , defined as

$$u_p \equiv \frac{a^4}{6\tilde{V}} \sum_p \frac{1}{N_c} \text{ReTr}(U_p). \quad (23)$$

Thanks to the relation  $E = 6\tilde{V}(1 - u_p)/a^4$ , the (partial) distribution function,  $P_\beta(u_p)$ , can be expressed as a function of  $E = S$ , and defined in terms of the density of states  $\rho(E)$  as follows:

$$P_\beta \left( u_p = 1 - \frac{a^4}{6\tilde{V}} E \right) = \rho(E) \frac{e^{-\beta E}}{Z(\beta)}, \quad (24)$$

where  $Z(\beta)$  is the partition function, Eq. (3). In proximity of the critical region of parameter space, for a system that undergoes a first-order phase transition between two possibly local vacua, we expect that the distribution function display a characteristic double-peak structure. The two values of the energy,  $E_\pm = 6\tilde{V}(1 - u_{p\pm})/a^4$ , at which  $P_\beta(u_p)$  is maximal, determine the energy of the two phases. On a finite volume  $\tilde{V}$ , we define the critical temperature  $T = T_c$  (and hence  $\beta = \beta_c$ , as we are keeping the volume fixed while changing the coupling  $\beta$ ) as the temperature at which the system tunnels between configurations in different phases with the same rate in either direction. Hence, the peaks must have equal height, and the relation

$$P_{\beta_c}(u_{p+}) = P_{\beta_c}(u_{p-}) \quad (25)$$

can be used to determine the critical coupling  $\beta_c$ .

As the temperature,  $T$ , of the gauge theory is a function of  $\beta$ , we recast the derivative with respect to  $T$  in Eq. (21) as a derivative with respect to  $\beta$ , following Ref. [86]. Direct calculation of the energy density requires the computation of Karsch coefficients [167], which is outside the scope of this work. However, assuming a vanishing pressure gap, as motivated by Ref. [145], the latent heat can be related to the plaquette jump,  $\Delta \langle u_p \rangle_{\beta_c} = |u_{p+} - u_{p-}|$ , via

$$\frac{L_h}{T_c^4} = - \left( 6N_c^4 a \frac{\partial \beta}{\partial a} \Delta \langle u_p \rangle_\beta \right)_{\beta=\beta_c}, \quad (26)$$



where  $a(\partial\beta/\partial a)$  can be calculated by setting the scale—see the discussion leading to Eq. (35) of Ref. [86]. In this work we focus on the calculation of the plaquette jump.

We define the effective potential,  $W_\beta(E)$ , as

$$W_\beta(E) \equiv -\log\langle\delta(S - E)\rangle_\beta = -\log P_\beta(E). \quad (27)$$

At criticality,  $W_\beta(E)$  displays two degenerate minima at the values of  $E$  of the equilibrium states of the two coexisting phases.<sup>1</sup>

The quantum system defined in Eq. (1) can be said to have internal energy  $E$  and entropy  $s = \log \rho(E)$ , following the prescription of the microcanonical ensemble. We then define a temperature  $t$  as  $1/t(E) \equiv \partial s / \partial E$ , in analogy with thermodynamics, and the free energy  $F$  as the Legendre transform

$$F(t) \equiv E - ts. \quad (28)$$

All the quantities mentioned above can be estimated from the approximate density of states  $\rho(E) \simeq \tilde{\rho}(E)$ . In particular, thanks to Eq. (5), the entropy for  $E \simeq E_n$  is

$$s(E \simeq E_n) = c_1 + \frac{\Delta E}{4}(a_1 + a_n) + \frac{\Delta E}{2} \sum_{k=2}^{n-1} a_k + a_n(E - E_n), \quad (29)$$

and the corresponding temperature is hence

$$t = \frac{1}{a_n}. \quad (30)$$

The computation of  $s(E)$  (and of  $F(t)$ ), is affected by an ambiguity on the value of  $c_1$ , as mentioned at the end of Sec. II. This ambiguity can in principle be fixed by requiring that  $s(E)$  be positive for all  $E$  and vanish as  $t \rightarrow 0$ .

Our estimate  $\tilde{\rho}$  is obtained by computing the sequence of values  $\{a_n\}_{n=1}^{2N-1}$  using the LLR algorithm, as outlined in Sec. II. The LLR parameters chosen for this work are shown in Table II. Note that in the specific application studied here NR iterations were considered unnecessary, hence  $\tilde{m} = 0$ . Once  $\tilde{\rho}$  is known, all relevant observables are known as well, by using the relations reported in this section.

There are two further numerical details worth discussing here, before we move onto presenting our results. Firstly, the LLR algorithm requires trial initial  $a_n$  vales. We have computed the average action for evenly spaced  $\beta$  values.

<sup>1</sup>If we replace  $E$ , which depends on  $u_p$ , with the extremal  $\langle E \rangle_\beta = \frac{6\tilde{V}}{a^4} (1 - \langle u_p \rangle_\beta)$ , for each  $\beta$ , then  $W_\beta(\langle E \rangle_\beta)$  is independent of  $\beta$ , and is a pure response function  $\langle E \rangle_\beta$ . In other words, this is the Legendre transform of the logarithm of the partition function  $Z(\beta)$ , in which  $\beta$  is the external source.

TABLE II. The LLR parameters used for this study.

Parameter	$\tilde{m}$	$\tilde{m}$	$n_{Th}$	$n_M$	$n_S$	$n_R$
Value	0	500	200	500	1	20

Linearly fitting this and inverting can give an initial estimate for the relation between  $a_n$  and  $E_n$ . The guess is then refined through a small number of RM iterations. The starting values  $\{a_n^{(0)}\}$  have been thus set for each energy interval over the relevant energy range of the system. The preliminary runs are also useful to locate the energy ranges  $[E_{\min}, E_{\max}]$  that are relevant to the study of the phase transition. On the basis of preliminary analyses we set  $a^4 E_{\min} / (6\tilde{V}) \approx 0.44$  and  $a^4 E_{\max} / (6\tilde{V}) \approx 0.46$ .

Second, for each  $n$ , the coefficient  $a_n$  is obtained by truncating the sequence  $\{a_n^{(m)}\}$  of RM updates at a value of  $m$  for which we expect the asymptotic  $1/\sqrt{m}$  behavior of the standard deviation to have set in. Due to the centrality of this behavior for the correct working of the algorithm, the corresponding test is the first numerical result we report in the next section.

## V. RESULTS

In order to verify the convergence of the Robbins-Monro algorithm, we study the distribution of the value of  $a_n^{(m)}$ , for each energy interval, as a function of the iteration

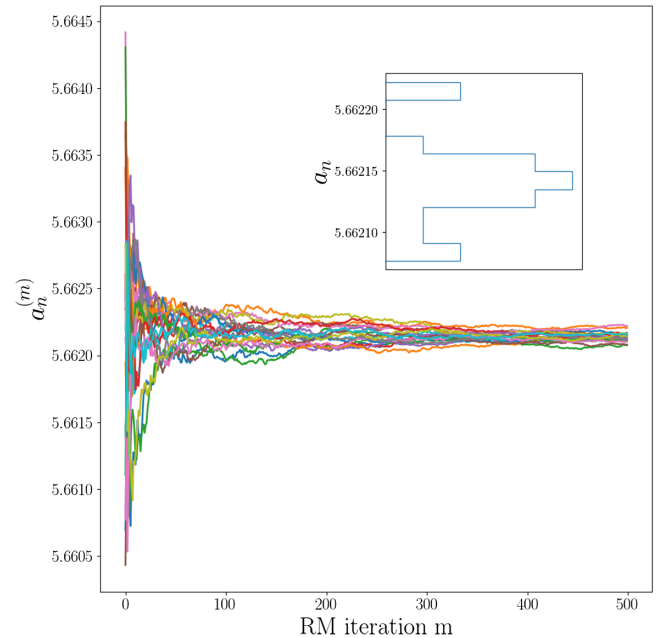


FIG. 1. Twenty histories of  $a_n^{(m)}$  as they are updated through 500 RM iterations, in different colors. This example is for a system with energy interval size  $a^4 \Delta E / (6\tilde{V}) = 0.0007$ , and the interval centered at  $u_p = 0.540676$ . The inset shows the distribution of the final  $a_n$  values.

TABLE III. The values of  $\Delta_E$  used for this analysis, for each choice of the number of intervals,  $2N - 1$ , in the energy range  $[E_{\min}, E_{\max}]$ . The four-dimensional lattice has space-time volume  $\tilde{V}/a^4 = 4 \times 20^3$ . Numerical values have been rounded to four decimal places for convenience.

$2N - 1$	$\frac{a^4}{6\tilde{V}} \Delta_E$	$\frac{a^4}{6\tilde{V}} E_{\min}$	$\frac{a^4}{6\tilde{V}} E_{\max}$
8	0.0063	0.4374	0.4659
15	0.0030	0.4380	0.4619
28	0.0015	0.4387	0.4604
55	0.0007	0.4391	0.4601
108	0.0004	0.4394	0.4598

number,  $m$ . An example of this process is displayed in Fig. 1, for the energy interval centered at  $a^4 E_n / (6\tilde{V}) = 0.459324$  ( $u_p = 0.540676$ ), with  $a^4 \Delta_E / (6\tilde{V}) = 0.0007$ . The figure shows in different colors twenty independent Robbins-Monro trajectories. The trajectories are characterized by large oscillations at small  $m$ , followed by convergence to a common value at large  $m$ . The distribution of the asymptotic behavior of the final values has standard deviation that scales as  $\sim 1/\sqrt{m}$ . On the basis of extensive test runs, we identified  $\tilde{m} = 500$  iterations of the RM algorithm as providing a good estimate of  $a_n$ . We verified that by this stage the twenty final estimates are normally distributed around their average value.

To extrapolate our results towards the  $\Delta_E \rightarrow 0$  limit, we vary the number of subintervals  $2N - 1$ , and repeat the process of computing the estimates of  $a_n^{(m)}$ . The corresponding values of  $a^4 \Delta_E / (6\tilde{V})$ , and of the intervals analyzed, are reported in Table III.

In Fig. 2, we show our measurements of  $a_n$ , with their uncertainty, as a function of  $u_p = 1 - a^4 E_n / (6\tilde{V})$ . The different curves show the results for several different values of  $\Delta_E$ . For  $\Delta_E$  sufficiently small [ $a^4 \Delta_E / (6\tilde{V}) \leq 0.0030$ ], a characteristic limiting shape starts to emerge in  $a_n$  as a function of  $u_p$ , with the presence of one local minimum, one local maximum, and an inflection point between them. The resulting noninvertibility of  $a_n(u_p)$  is closely related to the qualitative features of  $P_\beta(u_p)$ , as discussed in Sec. IV, and to the presence of a first-order phase transition. Setting  $\Delta_E$  to smaller values, the curve  $a_n(u_p)$  becomes smoother, which reduces the magnitude of the systematic error due to  $\Delta_E$  itself.

The probability distribution of the average plaquette is obtained from Eq. (24). Estimates of  $P_\beta(u_p)$  are displayed in Fig. 3. The solid blue lines are our results, obtained using the LLR method. We compare them directly with the orange dashed lines obtained by using the standard importance sampling approach. Agreement between the two is evident, yet small discrepancies are visible in the neighborhood of the maxima and of the local minimum of  $P_\beta(u_p)$ . We show a number of examples displaying a single peak,

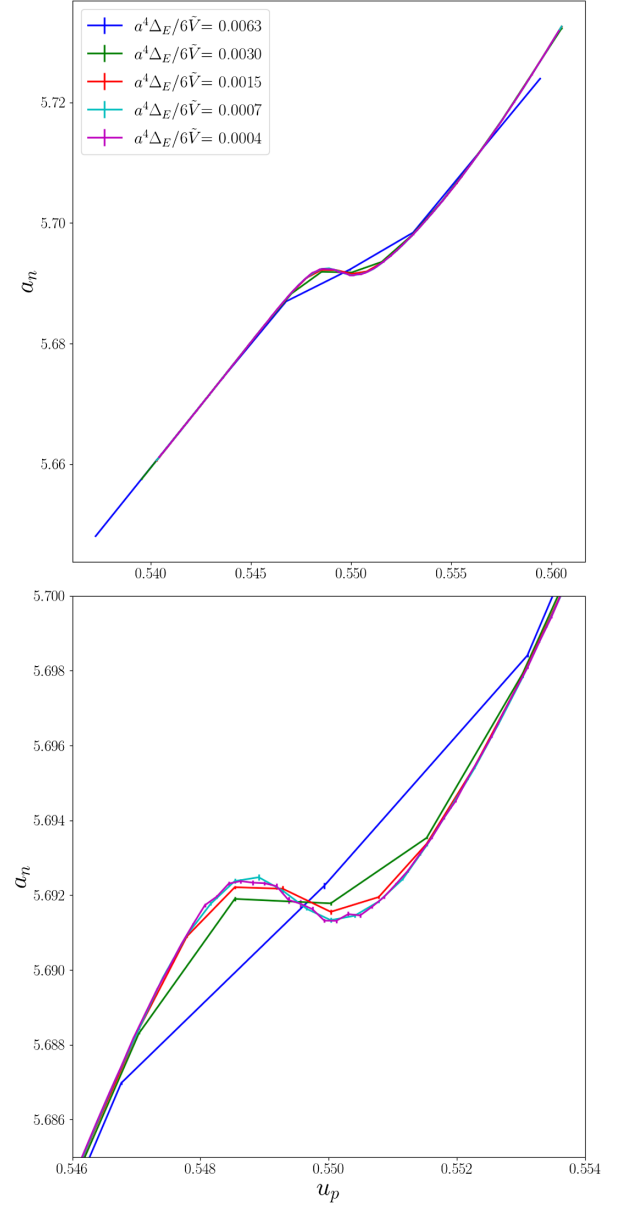


FIG. 2. Measurements of  $a_n$ , plotted against  $u_p$  at the center of the energy intervals. Errors are estimated by bootstrapping over 20 repeats. Each value of  $a_n$  is the final result of 500 iterations of the Robbins-Monro algorithm, for a lattices with  $\tilde{V}/a^4 = 4 \times 20^3$ . The different curves/colors refer to different choices of  $\Delta_E$ —see Table III—with the roughest results corresponding to the largest choices of  $\Delta_E$ . The bottom panel is a detail of the top one, focusing on the region in which  $a_n(u_p)$  is not invertible.

but for  $\beta = 5.69187$  two peaks of similar height are present. As explained in Sec. IV, this is the expected signal of a first-order phase transition.

As discussed in Sec. II, after each RM update, configuration swaps are considered, to ensure ergodicity of the algorithm. Figure 4 shows the evolution of the full set of  $\{a_n\}_{n=1}^{2N-1}$  against the RM iteration,  $m$ . Following the track of the colors on the diagram shows how the configurations

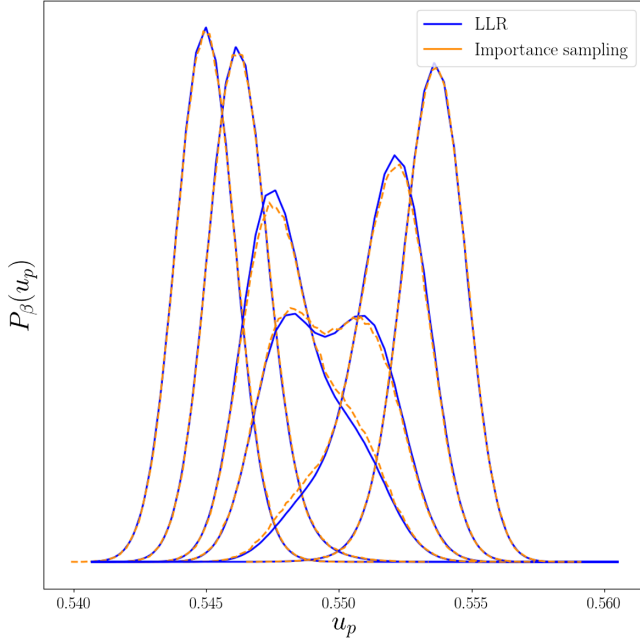


FIG. 3. The probability distribution,  $P_\beta(u_p)$ , computed with LLR method with  $a^4\Delta_E/\tilde{V} = 0.0007$  and  $\tilde{V}/a^4 = 4 \times 10^3$  (solid blue), compared to the same probability distribution computed with the standard lattice method based upon importance sampling (dashed orange). The probability density for different values of the coupling  $\beta$  are shown, from left to right:  $\beta = 5.68000$ ,  $\beta = 5.68500$ ,  $\beta = 5.69000$ ,  $\beta = 5.69187$ ,  $\beta = 5.69500$ , and  $\beta = 5.70000$ .

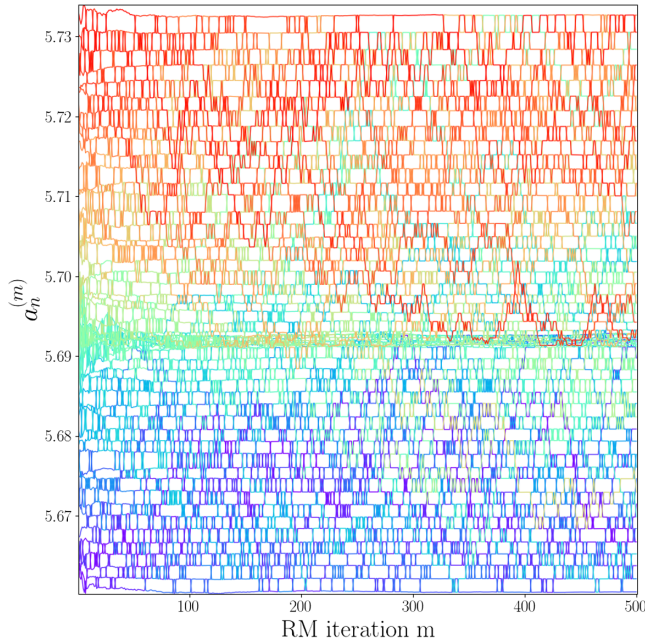


FIG. 4. The trajectories of the set  $\{a_n\}_{n=1}^{2N-1}$  are shown for 500 Robbins-Monro updates for a single run with configuration swaps included, for  $a^4\Delta_E/(6\tilde{V}) = 0.0007$ . The colors are determined by the energy interval that a given lattice system started in and follow them as they are exchanged between energy intervals.

are swapped. The clustering of values around  $a_n \sim 5.692$  is due to noninvertibility of  $a_n(u_p)$  in the critical region. The diagram shows that, although in general terms there is an appreciable rate of exchange of configurations, it appears to be less probable to exchange configurations across the two different phases.

### A. Critical T and latent heat

The importance of the measurement of the critical value  $\beta_c$  and of the position of the peaks of  $P_{\beta_c}(u_p)$  ( $u_{p+}$  and  $u_{p-}$ ) is explained in Sec. IV. In proximity of the transition at each value of  $\beta$ , a double Gaussian function can be fitted to  $P_\beta(u_p)$ , using the location of the local maxima and the width of the peaks as fitting parameters. The best-fit parameters are functions of  $\beta$ . An estimate of  $\beta_c$  can then be obtained by solving the equation  $|P_+ - P_-| = 0$ , where  $P_+ = P_\beta(u_{p+})$  and  $P_- = P_\beta(u_{p-})$ , with the bisection method. The numerical values of  $u_{p\pm}$  and  $\beta_c$  can then be used for the calculation of the latent heat through Eq. (26).

A representative example of the numerical results obtained from the LLR method, displaying also a fitted double Gaussian, is displayed in Fig. 5. The agreement between the numerical and fitted curves is very good, with small deviations only appearing at the boundaries of the interval of  $u_p$  depicted in the plot, which are not of primary importance in the fitting procedure.

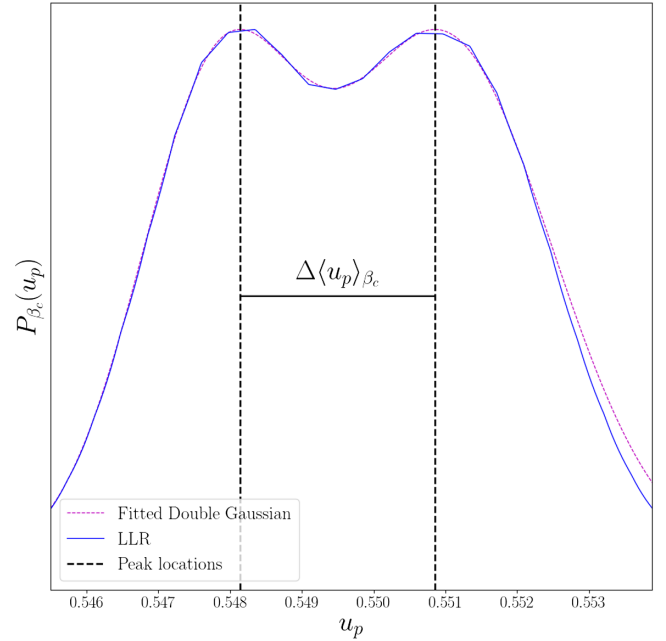


FIG. 5. The double-peak structure of the plaquette probability distribution,  $P_\beta(u_p)$ , for  $\beta = \beta_c = 5.69196$  tuned to the critical point for this specific LLR run, when the two peaks have equal height. A double Gaussian fitted at the peaks of the plots is shown in magenta (dashed), and compared with the blue (solid) line representing the LLR numerical results. We also show explicitly the location of the two peaks.

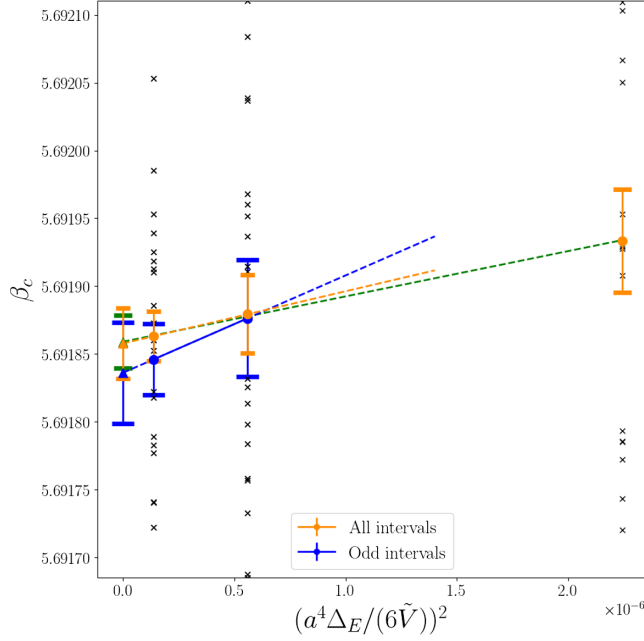


FIG. 6. Estimates of the critical coupling  $\beta_c$  as a function of the square of the energy interval,  $\Delta_E^2$ . The black crosses show the values of the critical coupling determined for each of the 20 repeats when all of the energy intervals are used in the determination of the plaquette distribution. The orange circles are the mean values of the black crosses and the error is found by bootstrapping them. The orange dashed line and triangle is a  $\Delta_E \rightarrow 0$  extrapolation of the two finest results when all intervals are included, while the green dashed line shows the extrapolation of all three points. The blue circles show results when only the odd numbered intervals are used  $\{a_{2n-1}, E_{2n-1}\}_{n=1}^N$ , an extrapolation to the  $\Delta_E \rightarrow 0$  limit is shown by the blue line and the blue triangle. The coarsest point included in this graph only contains a small number of intervals in the critical region, making the double-peak structure in the plaquette distribution difficult to resolve. All three final extrapolations are compatible with each other within errors.

Our estimates of  $\beta_c$  and  $\langle \Delta u_p \rangle_{\beta_c}$ , for each choice of  $\Delta_E$ , are displayed in Figs. 6 and 7. The numerical values are reported in Table IV. We perform a linear fit of the behavior of both  $\beta_c$  and  $\langle \Delta u_p \rangle_{\beta_c}$  as a function of  $\Delta_E^2$ . These fits are displayed in Figs. 6 and 7. We found the  $\chi^2$  of the linear fit to be much less than 1. The origin of its smallness lies in the large error in the determination of  $\beta_c$  at fixed  $\Delta_E$ . Several contributions to the errors of  $\beta_c$  have been carefully analyzed and accounted for, except for those originating from the correlation between different subintervals (leading to correlations across each set of  $a_n$ ) and the error on the fit of the double Gaussian itself. Calculations in different subintervals would indeed be completely independent, were it not for the configuration swapping, which is necessary to achieve ergodicity in the sampling of configuration space. Since canonical observables, such as  $P_\beta(u_p)$ , are determined from several values of  $a_n$ , they are affected by these

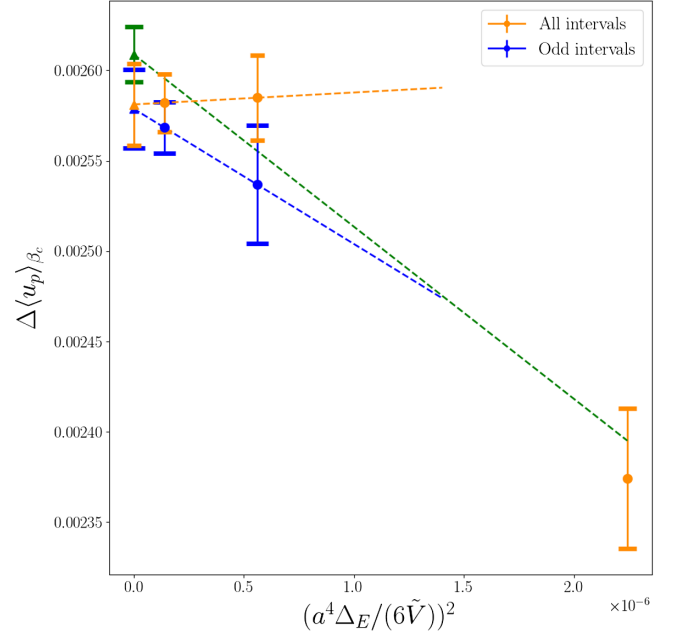


FIG. 7. Estimates of the plaquette jump at the critical point, the difference between the plaquette values at the two peaks of the plaquette distribution when the double-peak structure has peaks of equal height, as a function of the square of the energy interval,  $\Delta_E^2$ . The orange circles are the values found when all energy intervals are used to calculate the plaquette distribution, the error was found with a bootstrap procedure. The orange dashed line and triangle is an extrapolation of the two finest results when all intervals are included to the  $\Delta_E \rightarrow 0$  limit, while the green dashed line shows the extrapolation of all three points. The blue circles show results when only the odd numbered intervals are used  $\{a_{2n-1}, E_{2n-1}\}_{n=1}^N$ , an extrapolation to the  $\Delta_E \rightarrow 0$  limit is shown by the blue line and the blue triangle. The coarsest point included in this graph only contains a small number of intervals in the critical region, making the double peak structure difficult to resolve. All three final extrapolations are compatible with each other within errors.

autocorrelations. In order to approximately quantify the magnitude of these effects on the final estimate of  $\beta_c$ , we have computed this quantity from only half the  $a_n$  estimates, i.e. only computed using the nonoverlapping odd numbered energy intervals  $\{a_{2n-1}, E_{2n-1}\}_{n=1}^N$ . The coarsest example in the plot ( $a^4 \Delta_E / \tilde{V} = 0.0015$ ) has also been treated separately as it only contains a small number of intervals in the critical region. Extrapolations both including and excluding this point have been carried out, as well as an extrapolation using the points with only half the energy intervals. All extrapolations agree with one another within errors.

## B. Thermodynamic potentials

As discussed in Sec. IV, the LLR algorithm, through the estimation of  $\rho(E)$ , allows us to estimate the thermodynamic potentials of the bulk system. We focus our attention on the free energy,  $F$ , defined in Eq. (28), the entropy,



TABLE IV. The values of the critical coupling,  $\beta_c$ , and the difference between the peaks of the probability distribution at this coupling,  $\Delta\langle u_p \rangle_{\beta_c}$ , for different energy interval sizes  $\Delta_E$ . The table shows results obtained in two ways. Either all intervals are included or only the odd intervals,  $\{a_{2n-1}, E_{2n-1}\}_{n=1}^N$ . The symbol ‘ $\rightarrow 0$ ’ is used to denote the result of an extrapolation. The table contains three extrapolations. An extrapolation using the results when only odd intervals are considered, an extrapolation when all points with all the intervals are used and an extrapolation of the two finest interval sizes when all intervals are used. See also Ref. [86].

	$\frac{a^4 \Delta_E}{6V}$	$\beta_c$	$\Delta\langle u_p \rangle_{\beta_c}$
Odd intervals	0.0007	5.69188(4)	0.00254(3)
Odd intervals	0.0004	5.69185(3)	0.00257(2)
All intervals	0.0015	5.69193(4)	0.00237(4)
All intervals	0.0007	5.69188(3)	0.00258(2)
All intervals	0.0004	5.69186(2)	0.00258(2)
Odd intervals	$\rightarrow 0$	5.69184(4)	0.00258(2)
All intervals all points	$\rightarrow 0$	5.69186(3)	0.00258(2)
All intervals 2 points	$\rightarrow 0$	5.69186(2)	0.00261(2)

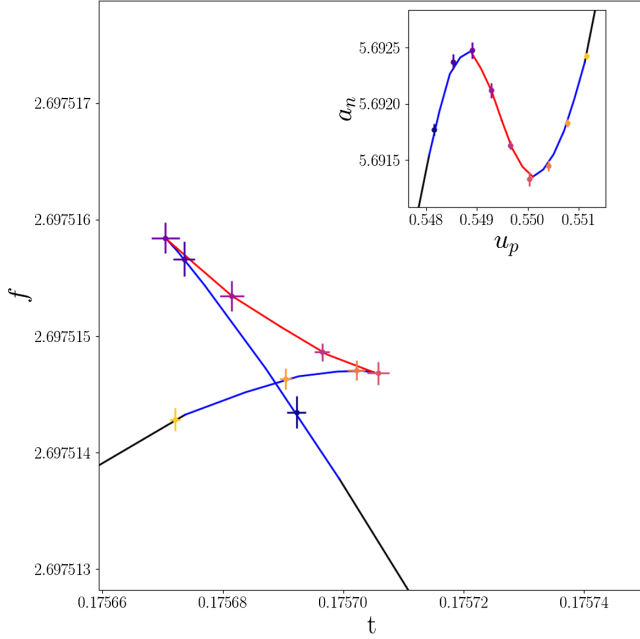


FIG. 8. The (subtracted) free energy,  $f$ , as a function of the (discretized, microcanonical) temperature  $t = 1/a_n$ .  $f$  is defined in the main body of the text. The dots (with errors) represent the values of  $f$  corresponding to the center of each energy interval used in the LLR algorithm, while the solid line is reconstructed by piecewise linearly interpolation of  $a_n(u_p)$ . The color coding of the points and solid lines are chosen to match those in the inset, displaying our numerical results for  $a_n(u_p)$ . In black we show the regions of  $t$  for which  $f$  is single valued, in blue we show the (meta)stable solutions within the region where  $f$  is multivalued, and in red the unstable (tachyonic) branch of solutions. The dots follow a colormap in the value average plaquette, with darker colors corresponding to smaller  $u_p$ .

$s$ , defined in Eq. (29), and the (microcanonical) temperature,  $t$ , in Eq. (30). As we showed explicitly in Fig. 2,  $a_n(u_p)$  and therefore  $t(E)$  is not globally invertible. Yet, we can study how  $F$  evolves as a function of  $t$ , by piecewise inverting  $t(E) \leftrightarrow E(t)$ .

In order to best expose the behavior of  $F(t)$ , we consider a *subtracted* free energy, defined as  $f = a^4(F(t) + \Sigma t)/(\tilde{V})$ . The constant  $\Sigma$ , as we anticipated after Eq. (30), reflects the existence of an arbitrary additive constant in  $s$ , which we are now removing, with an approximate numerical procedure. The subtracted free energy is displayed in Fig. 8, as a

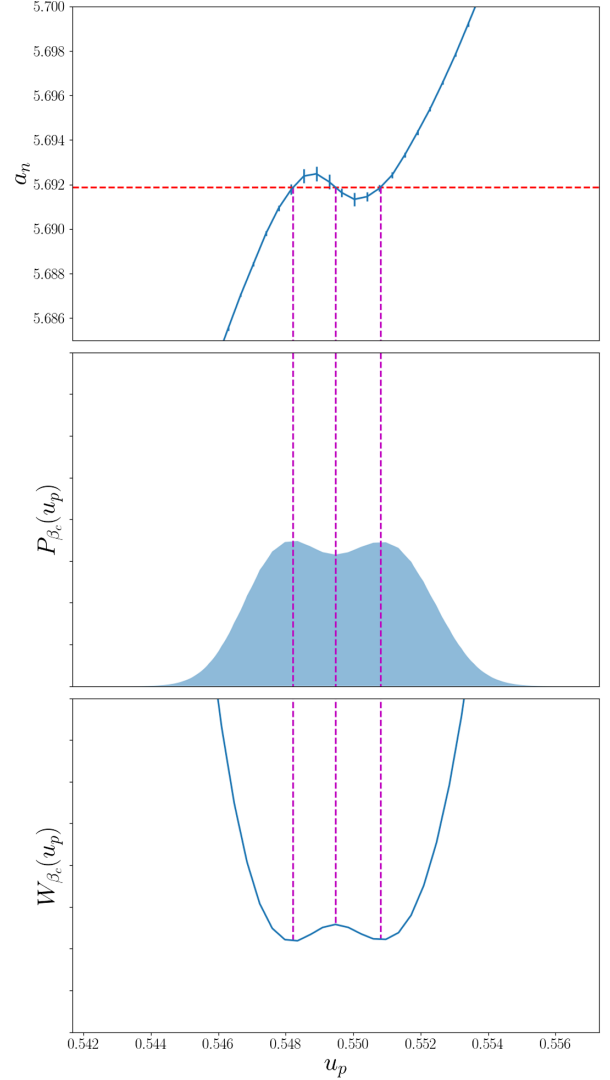


FIG. 9. Top panel:  $a_n (= 1/t_n)$  against  $u_p$  at the center of the energy intervals, in close proximity of the critical region. Middle panel: the reconstructed plaquette distribution,  $P_\beta(u_p)$ , at critical coupling  $\beta_c = 5.69187$ . Bottom panel: quantum effective potential for the plaquette at the critical coupling. The red line in the top plot shows the critical value of the coupling and its relation to the microcanonical temperature,  $a_n$ . The magenta (vertical, dashed) lines show the locations at which the red line intersects the curve  $a_n(u_p)$ .

function of (discretized)  $t = 1/a_n$ . For the purpose of producing this figure,  $\Sigma$  has been calculated as the average of the entropy over the interval of (microcanonical) temperatures displayed in the plot which would correspond to the average gradient of the curve. This rough estimate is not equivalent to imposing the third law of thermodynamics ( $\lim_{t \rightarrow 0} s = 0$ ), but suffices for our current purposes, and allows us to avoid the expensive process of repeating the LLR procedure for choices of  $E_n$  that lie far away from the critical region.

In Fig. 8, the uncertainty in the numerical extraction of  $a_n$  affects both axes of the plot. The values of  $f$  corresponding to the piecewise linear interpolation are represented in the main plot as colored lines. The plot clearly shows the multivalued nature of the free energy, the location of the temperature corresponding to criticality in the thermodynamic limit, and details about stable, metastable and tachyonic branches of configurations of the system. The discontinuity in the first derivative is located at  $t_c \simeq 0.175690$ , which is the temperature at which the system undergoes a first-order phase transition.

The relation between different branches of  $F(t)$  and physical stability is illustrated in Fig. 9. The inverse temperature  $a_n$  is displayed as a function of  $u_p = 1 - a^4 E_n / 6\tilde{V}$  in the top panel. The plaquette probability distribution at the critical point,  $P_{\beta_c}(u_p)$ , is depicted in the middle panel. The corresponding effective potential is plotted in the bottom panel. While the two configurations corresponding to maxima of  $P_{\beta_c}(u_p)$  are both absolute minima of the effective potential, a third configuration, corresponding to a local minimum of the probability, is a local maximum of the effective potential.

## VI. OUTLOOK

With this paper, we set the basis of a systematic research program that exploits the properties of the LLR method to yield future high-precision measurements characterizing lattice gauge theories in proximity of the confinement/deconfinement phase transition.<sup>2</sup> The method is powerful and promises to yield information that is difficult to access otherwise, as it modifies Monte Carlo sampling by restricting it to arbitrarily small energy windows. It hence provides numerical access to the details of the physics in regions of parameter space exhibiting all the typical features of first-order phase transitions: phase coexistence, metastability and/or instability of multiple branches of solutions, non-invertibility and/or multivaluedness of some state function.

We showed how the information from these energy-bound Monte Carlo feeds into recursive relations (e.g., an implementation of the Robbins-Monro algorithm) that can determine the density of states for any interesting range of

energies. And we provided explicit relations between the density of states and observables such as the critical temperature and the latent heat. Furthermore, we found that the results for the density of states can be recast in terms of an effective free energy and an effective potential that exhibit with spectacular level of resolution the details of the physics near the transition.

We restricted this study to the  $SU(3)$  lattice Yang-Mills theory, and performed it with one choice of lattice parameters, fixing  $N_L = 20$  and  $N_T = 4$ . The trademark of the LLR algorithm is that we found clear evidence of the first-order nature of the transition, without the need of a finite-volume study, and an extrapolation of the scaling to large volumes. The physically interesting observables need to be extrapolated to the continuum and infinite-volume limits, with dedicated, extensive numerical work, which would allow for a direct comparison with results that use different numerical techniques. In the future we plan to repeat the process with larger values of both  $N_T$  and  $N_L$ , which will provide us with control over lattice systematics.

We plan to apply this process to other theories, in particular those based on the sequence of symplectic groups  $Sp(2N)$ , which might play an important role in models of dark matter, and hence in the physics of the early Universe, by yielding a potentially detectable stochastic background of gravitation waves. In particular, the precise measurement of the effective potential,  $W_{\beta}(u_p)$ , the results of which are exemplified in Fig. 9, can be used to obtain a precise determination not just of the parameter,  $\alpha$ , controlling the strength of the phase transition, but also of the inverse duration of the transition,  $\beta/H_*$ . The latter is challenging to estimate from first principle, yet it is necessary in the calculation of the power-spectrum of stochastic gravitational waves,  $h^2\Omega_{\text{GW}}$ .

There are still some limitations to what we are able to do at this stage of development of this technique, and we would like to address them in the future. The first such challenge has to do with scalability and parallelization of the algorithm and software: the attentive reader will certainly be aware of the fact the energy constraint we are imposing is globally defined on the whole lattice configuration, a constraint that cannot be immediately parallelized, because it requires communication between different parallel subprocesses. This obstruction can be circumvented by partitioning the system in domains, and allowing for the information about the total energy to be shared across processes living in separate domains. But optimization of this process is a nontrivial open problem. Related to scalability is also the fact that when we tested the algorithm on larger volumes, we found a weakening of the transition, which makes it more difficult to detect. Whether this is an intrinsic feature of the algorithm, or a consequence of the choice of theory— $SU(3)$  is believed to undergo a weak first-order phase transition—is an open problem.

<sup>2</sup>See Refs. [160–162] for early results of studies that use a similar approach.

Finally, a more conceptual set of questions arises in view of applications; we showed that we can compute an effective potential, without the need to build an intermediate effective field theory treatment based on simplifying assumptions for the functional dependence on the order parameter. It would be useful to understand how this feature can be exploited for phenomenological purposes. For example, is the detailed knowledge of the effective potential going to improve current understanding of the amplitude of gravitational waves arising in the early Universe?

All these and other interesting questions are left for what we foresee to become an interesting and original research program, which we are planning to develop in the near- and long-term future.

*Research Data Access Statement*—The data generated for this manuscript can be downloaded from Ref. [168]. The simulation code can be found from Ref. [169].

### ACKNOWLEDGMENTS

We would like to thank David Schaich, Felix Springer, Jong-Wan Lee, and Antonio Rago for discussions. The work of D. M. is supported by a studentship awarded by the Data Intensive Centre for Doctoral Training, which is funded by the STFC Grant No. ST/P006779/1. The work of DV is partly supported by the Simons Foundation under the program “Targeted Grants to Institutes” awarded to the Hamilton Mathematics Institute. The work of B. L. and M. P. has been supported in part by the STFC Consolidated Grants No. ST/P00055X/1 and No. ST/T000813/1. B. L. and M. P. received funding from the European Research Council (ERC) under the European Union’s Horizon 2020 research and innovation program under Grant Agreement No. 813942. The work of B. L. is further supported in part by the Royal Society Wolfson Research Merit Award No. WM170010 and by the Leverhulme Trust Research Fellowship No. RF-2020-4619. Numerical simulations have been performed on the Swansea SUNBIRD cluster (part of the Supercomputing Wales project) and AccelerateAI A100 GPU system, and on the DiRAC Data Intensive service at Leicester. The Swansea SUNBIRD system and AccelerateAI are part funded by the European Regional Development Fund (ERDF) via Welsh Government. The DiRAC Data Intensive service at Leicester is operated by the University of Leicester IT Services, which forms part of the STFC DiRAC HPC Facility ([170]). The DiRAC Data Intensive service equipment at Leicester was funded by BEIS capital funding via STFC capital Grants No. ST/K000373/1 and No. ST/R002363/1 and STFC DiRAC Operations Grant No. ST/R001014/1. DiRAC is part of the National e-Infrastructure.

### APPENDIX A: CONSTRAINT-PRESERVING UPDATE PROPOSALS

In this appendix, we present our strategy for sampling random configurations from the probability density

$$dP_c(U) \propto dP(U)\theta(E - E_{n-1})\theta(E_{n+1} - E), \quad (\text{A1})$$

where  $dP(U)$  is the unconstrained probability density associated to the link variable  $U$ , and the  $\theta$  functions that implement the energy constraints,  $E_{n-1} = E_n - \Delta_E/2 \leq E \leq E_n + \Delta_E/2 = E_{n+1}$ .

The problem of sampling  $dP(U)$  has been elegantly solved in Ref. [171] for the gauge group  $SU(2)$ , and then generalized to  $SU(N_c)$  gauge groups in Ref. [172]. In the case  $N_c = 2$ ,

$$dP(U) \propto dU \exp \left\{ -\frac{\beta}{2} \text{Re}[\text{Tr}(U U_\square)] \right\}, \quad (\text{A2})$$

where  $U_\square$  is the *staple* around  $U$ , and  $dU$  is the Haar measure of the gauge group. Any  $SU(2)$  matrix  $U_p/k = U U_\square/k$  can be parametrized as  $U_p/k = u_0 \mathbb{I}_2 + i \vec{u} \cdot \vec{\tau}$ , where  $\vec{\tau}$  are the Pauli matrices,  $u_\mu$  are real numbers satisfying the normalization  $\sum_\mu u_\mu^2 = 1$  and  $k \equiv \det(U_\square)$ . The matrix  $U_p/k$  is obtained by first sampling  $\vec{u}$  uniformly on a sphere of radius  $\sqrt{1 - u_0^2}$ , and then  $u_0$  from the probability distribution

$$d\tilde{P}(u_0) \sim du_0 \sqrt{1 - u_0^2} \exp \{ \beta k u_0 \}. \quad (\text{A3})$$

We determine  $u_0$  as

$$u_0 = \frac{1}{\beta k} \log \left( e^{-\beta k} + \xi (e^{\beta k} - e^{-\beta k}) \right), \quad (\text{A4})$$

where  $0 \leq \xi \leq 1$  is a uniform random variable, and then perform an accept-reject step to correct for the presence of the factor  $\sqrt{1 - u_0^2}$  in Eq. (A3).

We further generalize these ideas to take into account, in the Monte Carlo evolution, the presence of the constraints  $E_{n-1} \leq E \leq E_{n+1}$ . Consider the variation in the total energy  $E$  due to the update of a specific link variable. Let  $E_i$  ( $E_f$ ) be this energy contribution before (after) the update. The energy constraints after the update are

$$E_{n-1} \leq E - E_i + E_f \leq E_{n+1}. \quad (\text{A5})$$

Since  $E_f = 2(d - 1) - k u_0$ , where  $d$  is the number of space-time dimensions, the above constraint can be expressed as  $u_{\min} < u_0 < u_{\max}$  where

$$u_{\min} = \max \left( \frac{2(d - 1) + (E - E_{n+1}) - E_i}{k}, -1 \right), \quad (\text{A6})$$

$$u_{\max} = \min \left( \frac{2(d - 1) + (E - E_{n-1}) - E_i}{k}, 1 \right). \quad (\text{A7})$$

These constraints can be enforced on the random sampling of  $u_0$  by setting

$$u_0 = \frac{1}{\beta k} \log \left( e^{\beta k u_{\min}} + \xi (e^{\beta k u_{\max}} - e^{\beta k u_{\min}}) \right), \quad (\text{A8})$$

where, as in Eq. (A4),  $0 \leq \xi \leq 1$  is sampled uniformly, and an accept-reject step is performed to correct for the presence of the factor  $\sqrt{1 - u_0^2}$ .

The constrained heat-bath algorithm outlined above can be generalized to  $SU(N_c)$  gauge groups following the Cabibbo-Marinari process suggested in Ref. [172]. The contribution of each  $SU(2)$  subgroup of a  $SU(N_c)$  link variable to the total energy of the system is additive. Thus, the constraint can be solved independently for each  $SU(2)$  subgroup of each link variable. It is easy to show that the constrained probability density of  $U$  is invariant under  $U \rightarrow \alpha_k U$ , where  $\alpha_k$  is an element of one of the  $SU(2)$  subgroups of  $SU(N_c)$ .

## APPENDIX B: FURTHER TECHNICAL DETAILS ON THE ALGORITHM AND PARALLELISM

To improve the scalability of the LLR algorithm when moving to larger lattice sizes, domain decomposition was implemented, in which the full lattice is split into subdomains, which can be processed separately. The restricted heat-bath updates, discussed in Appendix A, require prior knowledge of the total action of the system and will change

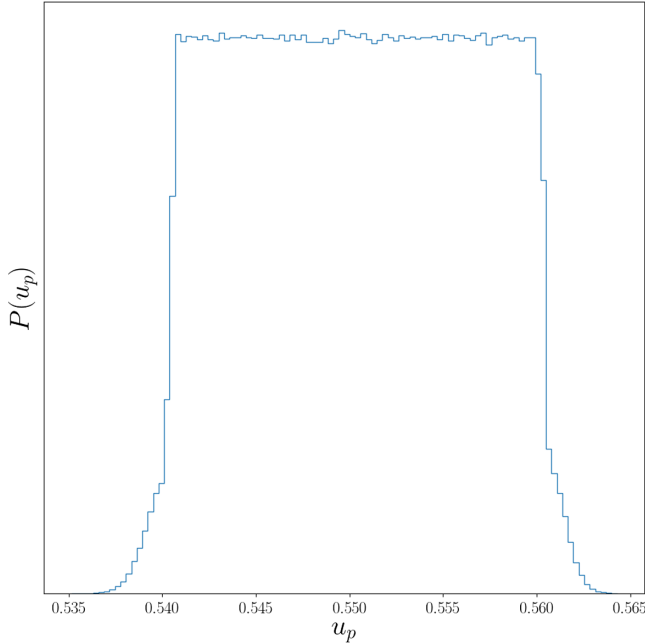


FIG. 10. For one LLR run with  $a^4 \Delta_E / 6\tilde{V} = 0.0007$ , the distribution of measured average plaquette values for all intervals is plotted for configurations restricted to a given energy interval, updated with a fixed value of  $a_n$ . Within the plaquette range,  $a^4 E_{\min} / 6\tilde{V} \leq 1 - u_p \leq a^4 E_{\max} / 6\tilde{V}$ , the distribution is approximately flat, while the boundary intervals have Gaussian tails allowing configurations to escape the energy boundaries, resolving the residual ergodicity problems.

it's value. Therefore, the restricted heat-bath update cannot occur in multiple subdomains simultaneously.

To circumvent this issue, in this work, domain decomposition is instead built out of a combination of restricted local heat-bath updates and the inherently microcanonical over-relaxation updates. This ensures the value of the total action is only changed in one subdomain at a time. If we have a lattice with  $N_D$  subdomains, during each sweep, one domain is updated with a local heat-bath update, while the other  $N_D - 1$  subdomains use the over-relaxation. After each sweep, the subdomain using the local heat-bath update is changed. One full lattice update is completed once each subdomain has been updated once using local heat bath. Therefore, for each full update, each subdomain undergoes one local heat-bath update and  $N_D - 1$  over-relaxation updates. For this work we use  $N_D = 4$ .

As discussed in Sec. II, there is a residual ergodicity problem, due to hard energy cutoffs at the boundaries  $E_{\min}$  and  $E_{\max}$ . To avoid these problems, in the boundary intervals the boundary cutoffs are removed, allowing configurations in the first and final intervals to freely move into energies  $E < E_{\min}$  and  $E > E_{\max}$ , respectively. This is done by simply replacing  $E_{n+1}$  ( $E_{n-1}$ ) in Eq. (A6) with  $6\tilde{V}/a^4$  (0) in the final (first) interval.

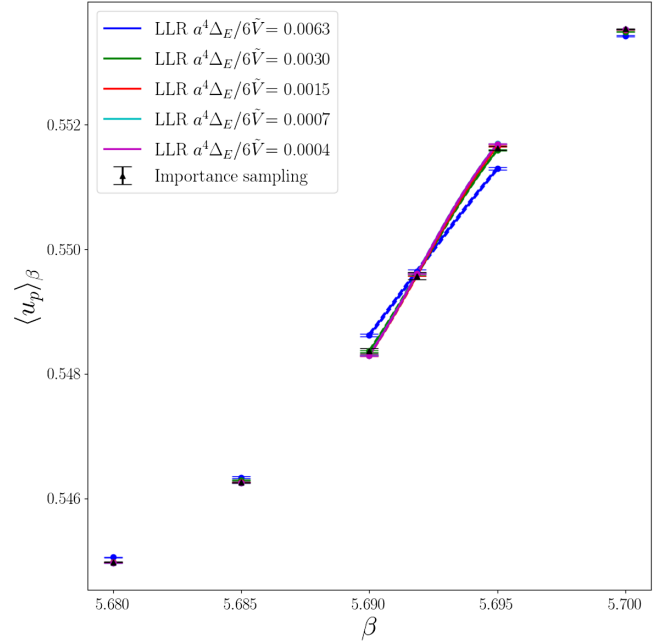


FIG. 11. The vacuum expectation value of the average plaquette for different couplings calculated using the LLR method for different  $a^4 \Delta_E / (6\tilde{V})$  sizes, and compared to the measurement from importance sampling methods (black triangles). In both cases the lattice size is  $\tilde{V}/a^4 = 4 \times 10^3$ . The dots are at a coupling with a direct comparison to the importance sampling. The solid lines are a finer scan around the critical region, containing 1000 points evenly spaced between 5.690 and 5.695. The errors on this line are calculated by bootstrapping over the repeats and are represented by the dashed curves.



Due to the removal of the hard energy cutoffs, the boundary intervals are no longer symmetric about the center of the interval. In this case, Eq. (13) cannot be used to update  $a_1$  and  $a_{2N-1}$ . Instead, we assume the boundaries are away from the critical region and the interval width is small, so the function  $E_n(a_n)$  is approximately linear. In this case we approximate,  $a_1 = 2a_2 - a_3$  and  $a_{2N-1} = 2a_{2N-2} - a_{2N-3}$ .

The sampled energy distribution of the boundary intervals are expected to be Gaussians centered at  $E_{2N-1}$  and  $E_1$ , with hard cutoffs at  $E_{2N-2}$  and  $E_2$ , respectively. The sampled plaquette distribution for all intervals, therefore, should be approximately flat within  $E_{\min} \leq E \leq E_{\max}$  with Gaussian tails on the boundaries. These expectations are confirmed by Fig. 10.

### APPENDIX C: $\Delta_E \rightarrow 0$ LIMIT

In the calculation of the observables there is a systematic error which is proportional to the size of the energy interval squared,  $\Delta_E^2$ , see Ref. [158]. To accurately represent an

expectation value and its error, we require that this systematic error be smaller than the statistical error, arising from repeating the determination of  $\{a_n\}_{n=1}^{2N-1}$ . To ensure  $\Delta_E$  is sufficiently small, in this section we analyze the  $\Delta_E \rightarrow 0$  limit for the average plaquette, the specific heat,

$$C_V(\beta) \equiv \frac{6\tilde{V}}{a^4} (\langle u_p^2 \rangle_\beta - \langle u_p \rangle_\beta^2), \quad (C1)$$

the Binder cumulant,

$$B_L(\beta) \equiv 1 - \frac{\langle u_p^4 \rangle_\beta}{3\langle u_p^2 \rangle_\beta^2}, \quad (C2)$$

the ensemble average of the absolute value of the Polyakov loop,  $\langle |L_p| \rangle_\beta$ , and the Polyakov-loop susceptibility,  $\chi_l(\beta)$ . We also take this limit for the maximum of the specific heat  $C_V^{(\max)}$  and the minimum of the Binder cumulant  $B_L^{(\min)}$ .

The observables calculated from the LLR method are compared against expectation values measured on a lattice of the same size ( $\tilde{V}/a^4 = 4 \times 20^3$ ) but obtained using

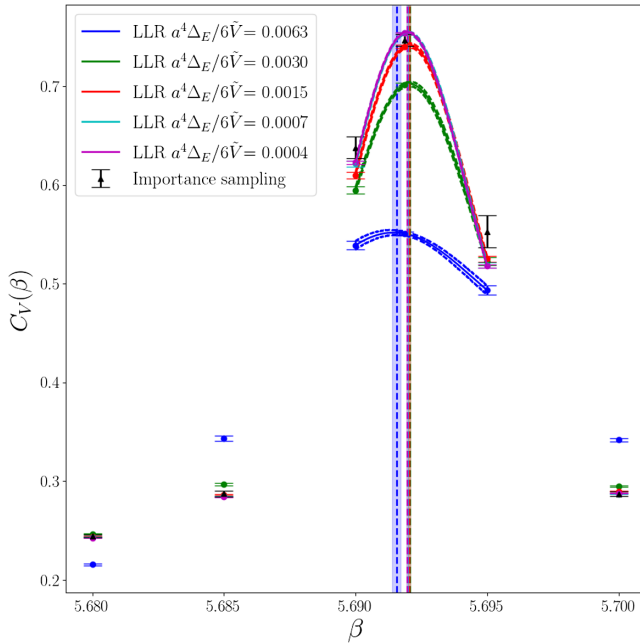


FIG. 12. The specific heat for different couplings calculated using the LLR method for different values of  $a^4\Delta_E/(6\tilde{V})$  sizes, and compared to the measurement from importance sampling methods (black triangles). In both cases the lattice size is  $\tilde{V}/a^4 = 4 \times 20^3$ . The dots are at a coupling with a direct comparison to the importance sampling. The solid lines are a finer scan around the critical region, containing 1000 points evenly spaced between 5.690 and 5.695. The errors on this line are calculated by bootstrapping over the repeats and are represented by the dashed curves. The extrema of the curve for all  $a^4\Delta_E/(6\tilde{V})$  sizes are shown by the vertical dashed lines, with the corresponding error represented by the shaded region. The extrema of all but the coarsest interval sizes overlap.

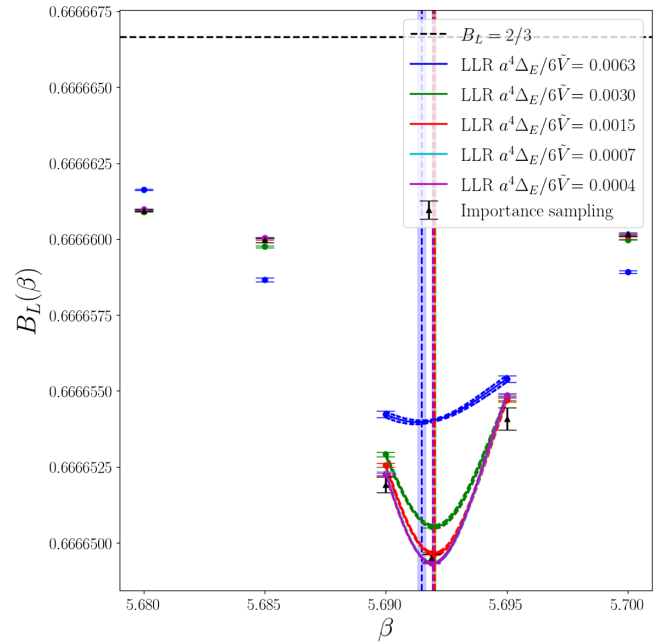


FIG. 13. The Binder cumulant for different couplings calculated using the LLR method for different values of  $a^4\Delta_E/(6\tilde{V})$  sizes, and compared to the measurement from importance sampling methods (black triangles). In both cases the lattice size is  $\tilde{V}/a^4 = 4 \times 20^3$ . The dots are at a coupling with a direct comparison to the importance sampling. The solid lines are a finer scan around the critical region, containing 1000 points evenly spaced between 5.690 and 5.695. The errors on this line are calculated by bootstrapping over the repeats and are represented by the dashed curves. The extrema of the curve for all  $a^4\Delta_E/(6\tilde{V})$  sizes are shown by the vertical dashed lines, with the corresponding error represented by the shaded region. The extrema of all but the coarsest interval sizes overlap.

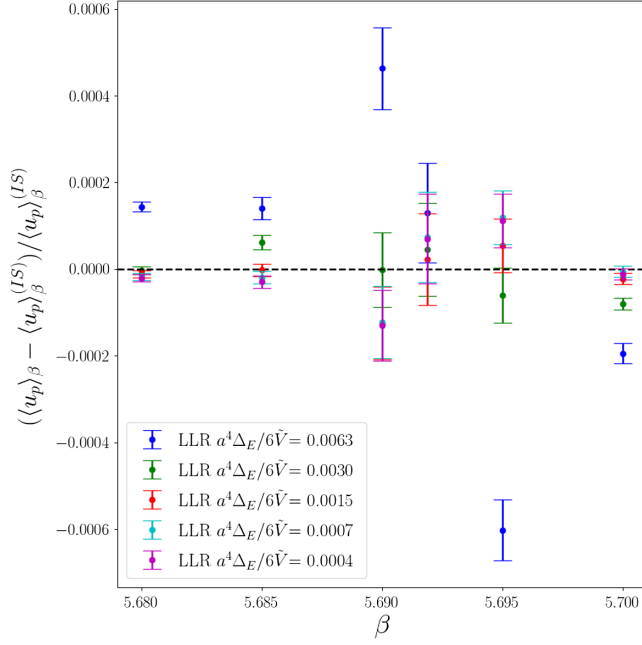


FIG. 14. The relative change for the vacuum expectation value of the average plaquette calculated between the LLR method and IS method results is shown at different couplings. In both cases the lattice size is  $\tilde{V}/a^4 = 4 \times 20^3$ . The colored dots show the results for different values of  $a^4\Delta_E/(6\tilde{V})$ . The errors were found by using bootstrap methods to calculate the error on LLR and importance sampling results separately, then propagating them.

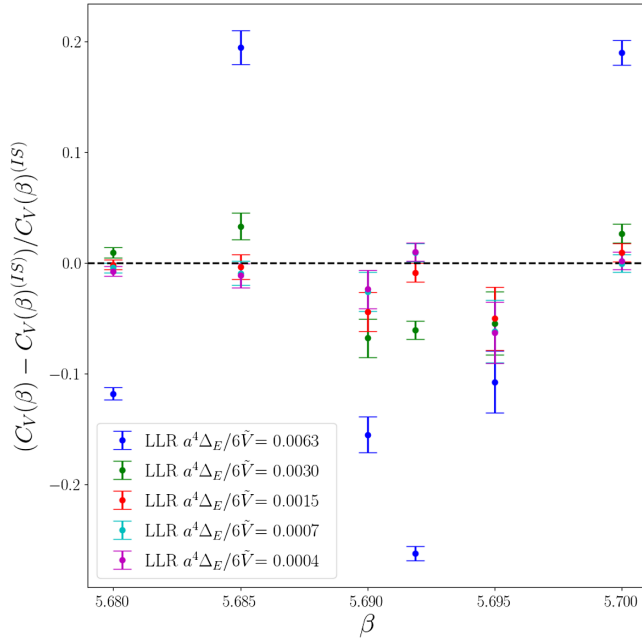


FIG. 15. The relative change for the specific heat calculated between the LLR method and IS method results is shown at different couplings. In both cases the lattice size is  $\tilde{V}/a^4 = 4 \times 20^3$ . The colored dots show the results for different values of  $a^4\Delta_E/(6\tilde{V})$ . The errors were found by using bootstrap methods on the LLR and importance sampling results separately, then propagating them.

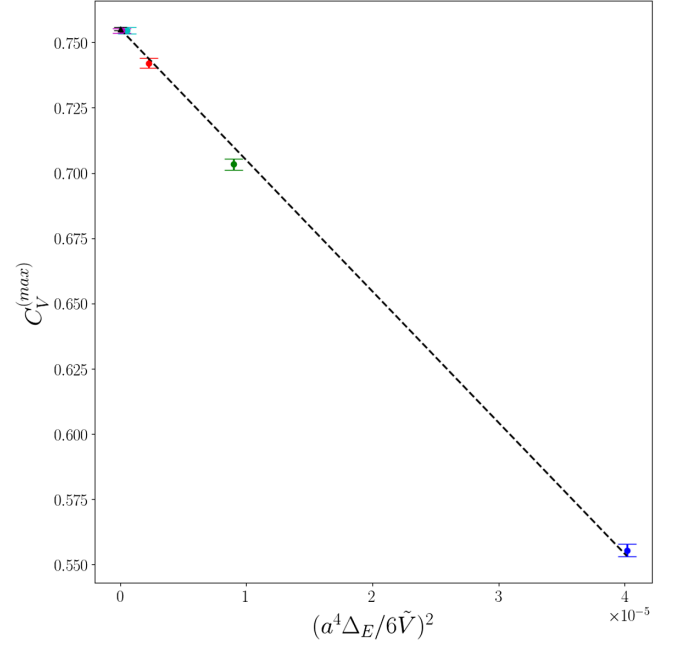


FIG. 16. The maximum value of the specific heat calculated using the LLR method for couplings around the critical region, containing 1000 points evenly spaced between 5.690 and 5.695, is plotted against the  $(a^4\Delta_E/(6\tilde{V}))^2$  value it was calculated at. The errors on each point are found by bootstrapping the repeats. The black dot shows the limit of  $(a^4\Delta_E/(6\tilde{V}))^2 \rightarrow 0$  and its errors, found by a linear fit. The lattice size is  $\tilde{V}/a^4 = 4 \times 20^3$ .

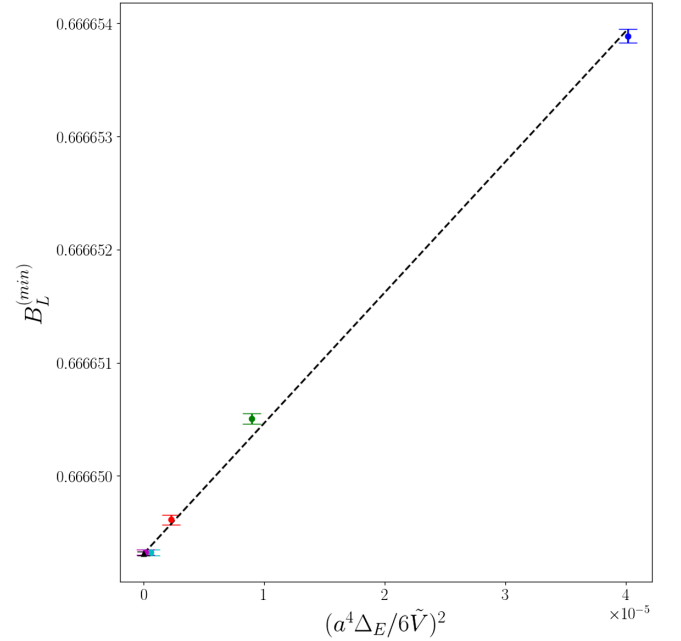


FIG. 17. The minimum value of the Binder cumulant calculated using the LLR method for couplings around the critical region, containing 1000 points evenly spaced between 5.690 and 5.695, is plotted against the  $(a^4\Delta_E/(6\tilde{V}))^2$  value it was calculated at. The errors on each point are found by bootstrapping the repeats. The black dot shows the limit of  $(a^4\Delta_E/(6\tilde{V}))^2 \rightarrow 0$  and its errors, found by a linear fit. The lattice size is  $\tilde{V}/a^4 = 4 \times 20^3$ .

standard importance sampling methods. The lattice was updated using 1 local heat bath update followed by 4 over-relaxation updates. At each coupling value, 500,000 measurements were taken, and the errors were computed using bootstrap methods.

The observables with explicit dependence on the energy,  $\langle u_p \rangle_\beta$ ,  $C_V(\beta)$ , and  $B_L(\beta)$ , are calculated using Eq. (4). The integral is computed over the entire possible energy range of the system. Since, the contribution from energy outside the range relevant for the problem is exponentially suppressed, the limits of the integral can be replaced with  $E_{\min}$  and  $E_{\max}$ . We then take the piecewise log-linear approximation for the density of states,  $\rho(E) \rightarrow \tilde{\rho}(E)$ , giving

$$\langle O \rangle_\beta = \frac{1}{Z_\beta} \sum_{n=1}^{2N-1} \int_{E_n - \Delta_E/4}^{E_n + \Delta_E/4} dE \tilde{\rho}(E) O(E) e^{-\beta E}. \quad (C3)$$

Using Eqs. (5) and (16), and taking all terms with no explicit  $E$  dependence outside the integral gives

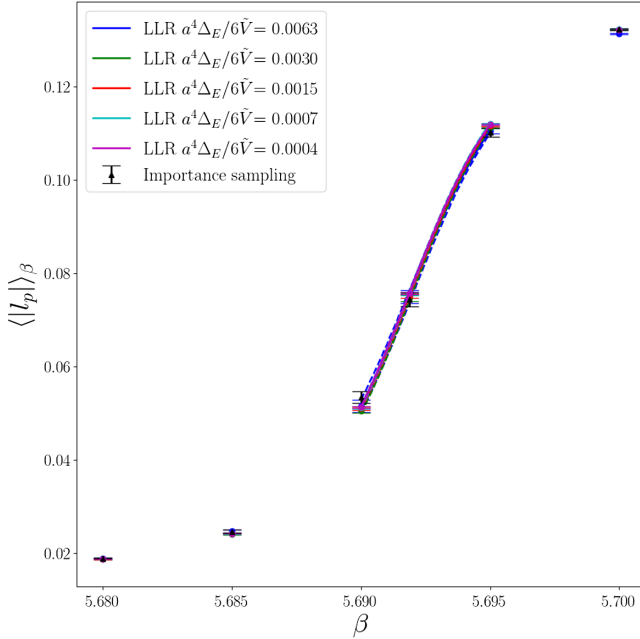


FIG. 18. The vacuum expectation value of the absolute value of the Polyakov loop for different couplings calculated using the LLR method for different values of  $a^4 \Delta_E / (6\tilde{V})$ , and compared to the measurement from importance sampling methods (black triangles). In both cases the lattice size is  $\tilde{V}/a^4 = 4 \times 20^3$ . The dots are at a coupling with a direct comparison to the importance sampling. The solid lines are a finer scan around the critical region, containing 100 points evenly spaced between 5.690 and 5.695. The errors on this line are calculated by bootstrapping over the repeats and are represented by the dashed curves. For the values determined with the LLR method, the calculation requires measurements of the Polyakov loop on a set of configurations found using the restricted energy updates, with  $a_n$  fixed to its final value. For these calculations 40,000 fixed  $a_n$  measurements were performed on all the intervals.

$$\langle O \rangle_\beta = \sum_{n=1}^{2N-1} \frac{\tilde{\rho}(E_n) e^{-\beta E_n}}{Z_\beta} \int_{-\Delta_E/4}^{\Delta_E/4} dE O(E + E_n) e^{E(a_n - \beta)}. \quad (C4)$$

By analytically solving the integral, inputting the desired coupling  $\beta$  and the obtained  $\{a_n\}$  values, we can therefore gain a numerical value for the expectation values.

The Polyakov loop and susceptibility depend on the configuration of the lattice ( $\phi$ ) rather than explicitly on the action, therefore they are calculated using Eq. (17). After the  $a_n$  values are found, a set of energy-restricted updates are carried out with  $a_n$  remaining fixed at its final value. On these configurations the action,  $S[\phi]$ , and observables of interest,  $B[\phi]$ , are calculated, giving access to the expectation value  $\tilde{B}[\phi]$ .

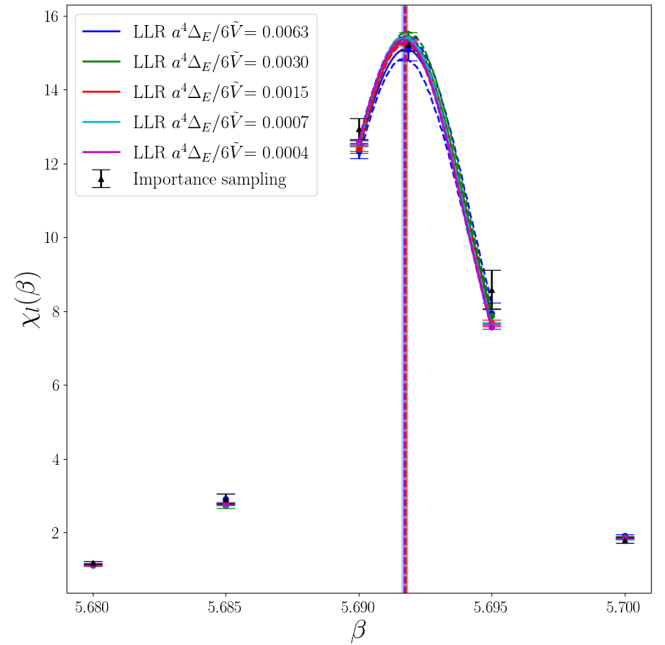


FIG. 19. The Polyakov-loop susceptibility for different couplings calculated using the LLR method for different values of  $a^4 \Delta_E / (6\tilde{V})$ , and compared to the measurement from importance sampling methods (black triangles). In both cases the lattice size is  $\tilde{V}/a^4 = 4 \times 20^3$ . The dots are at a coupling with a direct comparison to the importance sampling. The solid lines are a finer scan around the critical region, containing 100 points evenly spaced between 5.690 and 5.695. The errors on this line are calculated by bootstrapping over the repeats and are represented by the dashed curves. For the values determined with the LLR method, the calculation requires measurements of the Polyakov loop on a set of configurations found using the restricted energy updates, with  $a_n$  fixed to its final value. For these calculations 40,000 fixed  $a_n$  measurements were performed on all the intervals. The extrema of the curve for all  $a^4 \Delta_E / (6\tilde{V})$  sizes are shown by the vertical dashed lines, with the corresponding error represented by the shaded region. The extrema of all interval sizes overlap.

Figures 11–13 show the results for  $\langle u_p \rangle_\beta$ ,  $C_V(\beta)$ , and  $B_L(\beta)$ , respectively. In all cases the LLR results appear to converge to the curve obtained for the smallest interval. The results for the two smallest interval sizes are clearly consistent with each other.

The results for the smallest interval size follow the general trend of the values found using importance sampling. By plotting the relative change between expectation values of these observables and the importance sampling counterparts, Figs. 14 and 15, we see they are generally consistent within two standard deviations.

As discussed in Sec. V, for the smaller interval sizes the structure of  $a_n(E_n)$  is not invertible, giving rise to a probability distribution,  $P_\beta(u_p)$ , with a characteristic double-peak structure. However, for  $a^4\Delta_E/(6\tilde{V}) = 0.0063$ , the interval size is not sufficient to resolve this structure. As can be seen from the plots Figs. 11, 12, and 13, the behavior of the expectations of this ensemble is different. The peaks in the specific heat and the dip of the Binder cumulant are much shallower and the change in the plaquette much slower, making it consistent with a weaker transition or even a second order transition.

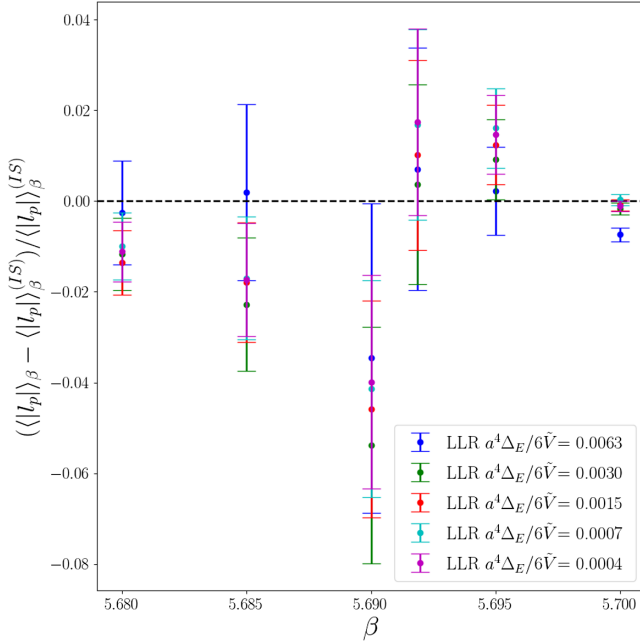


FIG. 20. The relative change in the vacuum expectation value of the absolute value of the Polyakov loop, calculated between the LLR method and the IS method results, is shown at different couplings. In both cases the lattice size is  $\tilde{V}/a^4 = 4 \times 20^3$ . The colored dots show the results for different values of  $a^4\Delta_E/(6\tilde{V})$ . The error is found by using bootstrap methods on LLR and importance sampling results separately, then propagating them. For the values determined with the LLR method, the calculation requires measurements of the Polyakov loop on a set of configurations found using the restricted energy updates, with  $a_n$  fixed to its final value. For these calculations 40,000 fixed  $a_n$  measurements were performed on all the intervals.

The location of the extrema of the specific heat and Binder cumulant, in the limit of  $\Delta_E \rightarrow 0$ , are shown in Figs. 16 and 17, respectively. A linear fit has been taken in  $(a^4\Delta_E/6\tilde{V})^2$ , and the results have been extrapolated to  $\Delta_E = 0$ . In both cases, the phase transition appears to become stronger as the critical region becomes better resolved with decreasing  $\Delta_E$ . In both plots the two smallest interval sizes appear to be consistent with each other and the extrapolation.

The results for  $\langle |l_p| \rangle_\beta$  and  $\chi_l(\beta)$  are shown in Figs. 18 and 19. The relative change between LLR and importance sampling results are shown in Figs. 20 and 21. Once more, the results converge to those of the smallest interval size and show good agreement with importance sampling ones. For these observables, the discrepancy between the largest interval and the others is small.

We report in Table V the values of the pseudocritical couplings identified by the extrema of the observables discussed in this appendix and by the equal height of the peaks in the energy distribution for the two finest values of  $\Delta_E$ . Our results show consistency across the definitions we have studied and good agreement between the values at the two  $\Delta_E$  for fixed observable.

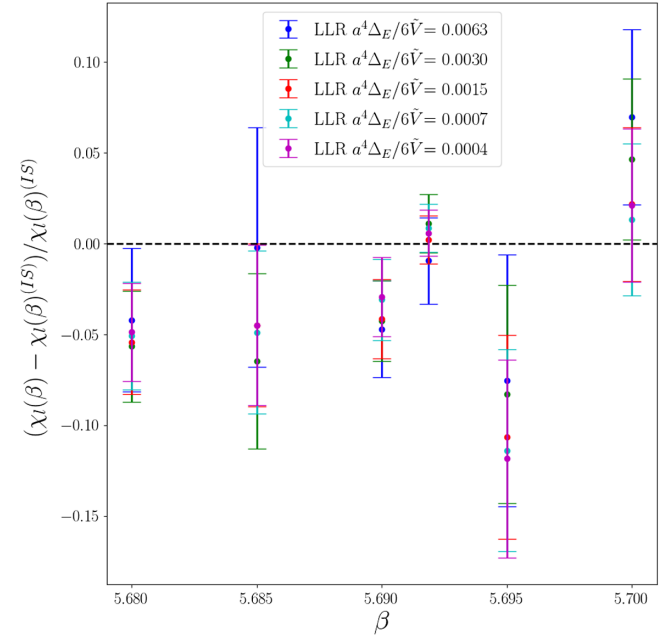


FIG. 21. The relative change in the Polyakov loop susceptibility, calculated between the LLR method and importance sampling (IS) method results, is shown at different couplings. In both cases the lattice size is  $\tilde{V}/a^4 = 4 \times 20^3$ . The colored dots show the results for different values of  $a^4\Delta_E/(6\tilde{V})$ . The error is found by using bootstrap methods on LLR and importance sampling results separately, then propagating them. For the values determined with the LLR method, the calculation requires measurements of the Polyakov loop on a set of configurations found using the restricted energy updates, with  $a_n$  fixed to its final value. For these calculations 40000 fixed  $a_n$  measurements were performed on all the intervals.



TABLE V. The values of the coupling,  $\beta$ , that correspond to the maximum of the specific heat,  $\beta(C_V^{(\max)})$ , the minimum of the binder cumulant,  $\beta(B_L^{(\min)})$ , and the maximum of the Polyakov loop susceptibility,  $\beta(\chi_l^{(\max)})$ , found by measuring the observables at a  $\beta$  values evenly spaced between 5.690 and 5.695. Measurements were carried out at  $1000\beta$  values for  $C_V$  and  $B_L$ , while for  $\chi_l$  100 values were scanned. These pseudocritical couplings are compared with the value presented in Sec. V, for the critical coupling,  $\beta_c$ . These results are for a  $SU(3)$  lattice of size  $\tilde{V}/a^4 = 4 \times 20^3$ , using the LLR method with interval sizes  $a^4\Delta_E/(6\tilde{V}) = 0.0007$  and  $0.0004$ .

$\frac{a^4\Delta_E}{6\tilde{V}}$	$\beta(C_V^{(\max)})$	$\beta(B_L^{(\min)})$	$\beta(\chi_l^{(\max)})$	$\beta_c$
0.0007	5.69198(3)	5.69194(3)	5.69170(3)	5.69188(3)
0.0004	5.69197(2)	5.69193(2)	5.69170(2)	5.69186(2)

In summary, all the tests reported in this appendix show that when the energy interval is small enough— $a^4\Delta_E/(6\tilde{V}) = 0.0007$  and  $0.0004$ —there is no discernible difference with the results of the extrapolation to zero interval, and general agreement is found with importance sampling.

- 
- [1] A. D. Sakharov, Violation of  $CP$  invariance, C asymmetry, and baryon asymmetry of the universe, *Pis'ma Zh. Eksp. Teor. Fiz.* **5**, 32 (1967).
  - [2] K. Kajantie, M. Laine, K. Rummukainen, and M. E. Shaposhnikov, Is there a hot electroweak phase transition at  $m_H \gtrsim m_W$ ?, *Phys. Rev. Lett.* **77**, 2887 (1996).
  - [3] F. Karsch, T. Neuhaus, A. Patkos, and J. Rank, Critical Higgs mass and temperature dependence of gauge boson masses in the  $SU(2)$  gauge Higgs model, *Nucl. Phys. B, Proc. Suppl.* **53**, 623 (1997).
  - [4] M. Gurtler, E.-M. Ilgenfritz, and A. Schiller, Where the electroweak phase transition ends, *Phys. Rev. D* **56**, 3888 (1997).
  - [5] K. Rummukainen, M. Tsypin, K. Kajantie, M. Laine, and M. E. Shaposhnikov, The universality class of the electroweak theory, *Nucl. Phys. B* **532**, 283 (1998).
  - [6] F. Csikor, Z. Fodor, and J. Heitger, Endpoint of the hot electroweak phase transition, *Phys. Rev. Lett.* **82**, 21 (1999).
  - [7] Y. Aoki, F. Csikor, Z. Fodor, and A. Ukawa, The endpoint of the first order phase transition of the  $SU(2)$  gauge Higgs model on a four-dimensional isotropic lattice, *Phys. Rev. D* **60**, 013001 (1999).
  - [8] M. D'Onofrio and K. Rummukainen, Standard model cross-over on the lattice, *Phys. Rev. D* **93**, 025003 (2016).
  - [9] M. Laine and K. Rummukainen, What's new with the electroweak phase transition?, *Nucl. Phys. B, Proc. Suppl.* **73**, 180 (1999).
  - [10] D. E. Morrissey and M. J. Ramsey-Musolf, Electroweak baryogenesis, *New J. Phys.* **14**, 125003 (2012).
  - [11] O. Gould, S. Güyer, and K. Rummukainen, First-order electroweak phase transitions: A nonperturbative update, *Phys. Rev. D* **106**, 114507 (2022).
  - [12] M. J. Strassler and K. M. Zurek, Echoes of a hidden valley at hadron colliders, *Phys. Lett. B* **651**, 374 (2007).
  - [13] K. Cheung and T.-C. Yuan, Hidden fermion as milli-charged dark matter in Stueckelberg  $Z'$  model, *J. High Energy Phys.* **03** (2007) 120.
  - [14] T. Hambye, Hidden vector dark matter, *J. High Energy Phys.* **01** (2009) 028.
  - [15] J. L. Feng, M. Kaplinghat, H. Tu, and H.-B. Yu, Hidden charged dark matter, *J. Cosmol. Astropart. Phys.* **07** (2009) 004.
  - [16] T. Cohen, D. J. Phalen, A. Pierce, and K. M. Zurek, Asymmetric dark matter from a GeV hidden sector, *Phys. Rev. D* **82**, 056001 (2010).
  - [17] R. Foot and S. Vagnozzi, Dissipative hidden sector dark matter, *Phys. Rev. D* **91**, 023512 (2015).
  - [18] G. Bertone and D. Hooper, History of dark matter, *Rev. Mod. Phys.* **90**, 045002 (2018).
  - [19] E. Del Nobile, C. Kouvaris, and F. Sannino, Interfering composite asymmetric dark matter for DAMA and CoGeNT, *Phys. Rev. D* **84**, 027301 (2011).
  - [20] A. Hietanen, R. Lewis, C. Pica, and F. Sannino, Composite Goldstone dark matter: Experimental predictions from the lattice, *J. High Energy Phys.* **12** (2014) 130.
  - [21] J. M. Cline, W. Huang, and G. D. Moore, Challenges for models with composite states, *Phys. Rev. D* **94**, 055029 (2016).
  - [22] G. Cacciapaglia, C. Pica, and F. Sannino, Fundamental composite dynamics: A review, *Phys. Rep.* **877**, 1 (2020).
  - [23] N. A. Dondi, F. Sannino, and J. Smirnov, Thermal history of composite dark matter, *Phys. Rev. D* **101**, 103010 (2020).
  - [24] S. Ge, K. Lawson, and A. Zhitnitsky, Axion quark nugget dark matter model: Size distribution and survival pattern, *Phys. Rev. D* **99**, 116017 (2019).
  - [25] V. Beylin, M. Y. Khlopov, V. Kuksa, and N. Volchanskiy, Hadronic and hadron-like physics of dark matter, *Symmetry* **11**, 587 (2019).

- [26] N. Yamanaka, H. Iida, A. Nakamura, and M. Wakayama, Dark matter scattering cross section and dynamics in dark Yang-Mills theory, *Phys. Lett. B* **813**, 136056 (2021).
- [27] N. Yamanaka, H. Iida, A. Nakamura, and M. Wakayama, Glueball scattering cross section in lattice SU(2) Yang-Mills theory, *Phys. Rev. D* **102**, 054507 (2020).
- [28] H. Cai and G. Cacciapaglia, Singlet dark matter in the SU(6)/SO(6) composite Higgs model, *Phys. Rev. D* **103**, 055002 (2021).
- [29] Y. Hochberg, E. Kuflik, T. Volansky, and J. G. Wacker, Mechanism for thermal relic dark matter of strongly interacting massive particles, *Phys. Rev. Lett.* **113**, 171301 (2014).
- [30] Y. Hochberg, E. Kuflik, H. Murayama, T. Volansky, and J. G. Wacker, Model for thermal relic dark matter of strongly interacting massive particles, *Phys. Rev. Lett.* **115**, 021301 (2015).
- [31] Y. Hochberg, E. Kuflik, and H. Murayama, SIMP spectroscopy, *J. High Energy Phys.* **05** (2016) 090.
- [32] N. Bernal, X. Chu, and J. Pradler, Simply split strongly interacting massive particles, *Phys. Rev. D* **95**, 115023 (2017).
- [33] A. Berlin, N. Blinov, S. Gori, P. Schuster, and N. Toro, Cosmology and accelerator tests of strongly interacting dark matter, *Phys. Rev. D* **97**, 055033 (2018).
- [34] N. Bernal, X. Chu, S. Kulkarni, and J. Pradler, Self-interacting dark matter without prejudice, *Phys. Rev. D* **101**, 055044 (2020).
- [35] Y.-D. Tsai, R. McGehee, and H. Murayama, Resonant self-interacting dark matter from dark QCD, *Phys. Rev. Lett.* **128**, 172001 (2022).
- [36] D. Kondo, R. McGehee, T. Melia, and H. Murayama, Linear sigma dark matter, *J. High Energy Phys.* **09** (2022) 041.
- [37] E. Witten, Cosmic separation of phases, *Phys. Rev. D* **30**, 272 (1984).
- [38] M. Kamionkowski, A. Kosowsky, and M. S. Turner, Gravitational radiation from first order phase transitions, *Phys. Rev. D* **49**, 2837 (1994).
- [39] B. Allen, The Stochastic gravity wave background: Sources and detection, in *Les Houches School of Physics: Astrophysical Sources of Gravitational Radiation* (Cambridge University Press, Cambridge, 1996), pp. 373–417, [arXiv:gr-qc/9604033](#).
- [40] P. Schwaller, Gravitational waves from a dark phase transition, *Phys. Rev. Lett.* **115**, 181101 (2015).
- [41] D. Croon, V. Sanz, and G. White, Model discrimination in gravitational wave spectra from dark phase transitions, *J. High Energy Phys.* **08** (2018) 203.
- [42] N. Christensen, Stochastic gravitational wave backgrounds, *Rep. Prog. Phys.* **82**, 016903 (2019).
- [43] N. Seto, S. Kawamura, and T. Nakamura, Possibility of direct measurement of the acceleration of the universe using 0.1-Hz band laser interferometer gravitational wave antenna in space, *Phys. Rev. Lett.* **87**, 221103 (2001).
- [44] S. Kawamura *et al.*, The Japanese space gravitational wave antenna DECIGO, *Classical Quantum Gravity* **23**, S125 (2006).
- [45] J. Crowder and N. J. Cornish, Beyond LISA: Exploring future gravitational wave missions, *Phys. Rev. D* **72**, 083005 (2005).
- [46] V. Corbin and N. J. Cornish, Detecting the cosmic gravitational wave background with the big bang observer, *Classical Quantum Gravity* **23**, 2435 (2006).
- [47] G. M. Harry, P. Fritschel, D. A. Shaddock, W. Folkner, and E. S. Phinney, Laser interferometry for the big bang observer, *Classical Quantum Gravity* **23**, 4887 (2006); **23**, 7361(E) (2006).
- [48] S. Hild *et al.*, Sensitivity studies for third-generation gravitational wave observatories, *Classical Quantum Gravity* **28**, 094013 (2011).
- [49] K. Yagi and N. Seto, Detector configuration of DECIGO/BBO and identification of cosmological neutron-star binaries, *Phys. Rev. D* **83**, 044011 (2011); **95**, 109901 (E) (2017).
- [50] B. Sathyaprakash *et al.*, Scientific objectives of Einstein Telescope, *Classical Quantum Gravity* **29**, 124013 (2012); **30**, 079501(E) (2013).
- [51] E. Thrane and J. D. Romano, Sensitivity curves for searches for gravitational-wave backgrounds, *Phys. Rev. D* **88**, 124032 (2013).
- [52] C. Caprini *et al.*, Science with the space-based interferometer eLISA. II: Gravitational waves from cosmological phase transitions, *J. Cosmol. Astropart. Phys.* **04** (2016) 001.
- [53] P. Amaro-Seoane *et al.* (LISA Collaboration), Laser interferometer space antenna, [arXiv:1702.00786](#).
- [54] B. P. Abbott *et al.* (LIGO Scientific Collaboration), Exploring the sensitivity of next generation gravitational wave detectors, *Classical Quantum Gravity* **34**, 044001 (2017).
- [55] S. Isoyama, H. Nakano, and T. Nakamura, Multiband gravitational-wave astronomy: Observing binary inspirals with a decihertz detector, B-DECIGO, *Prog. Theor. Exp. Phys.* **2018**, 073E01 (2018).
- [56] J. Baker *et al.*, The laser interferometer space antenna: Unveiling the millihertz gravitational wave sky, [arXiv:1907.06482](#).
- [57] V. Brdar, A. J. Helmboldt, and J. Kubo, Gravitational waves from first-order phase transitions: LIGO as a window to unexplored Seesaw scales, *J. Cosmol. Astropart. Phys.* **02** (2019) 021.
- [58] D. Reitze *et al.*, Cosmic Explorer: The U.S. contribution to gravitational-wave astronomy beyond LIGO, *Bull. Am. Astron. Soc.* **51**, 035 (2019).
- [59] C. Caprini *et al.*, Detecting gravitational waves from cosmological phase transitions with LISA: An update, *J. Cosmol. Astropart. Phys.* **03** (2020) 024.
- [60] M. Maggiore *et al.*, Science case for the Einstein Telescope, *J. Cosmol. Astropart. Phys.* **03** (2020) 050.
- [61] W.-C. Huang, M. Reichert, F. Sannino, and Z.-W. Wang, Testing the dark SU(N) Yang-Mills theory confined landscape: From the lattice to gravitational waves, *Phys. Rev. D* **104**, 035005 (2021).
- [62] J. Halverson, C. Long, A. Maiti, B. Nelson, and G. Salinas, Gravitational waves from dark Yang-Mills sectors, *J. High Energy Phys.* **05** (2021) 154.

- [63] Z. Kang, J. Zhu, and S. Matsuzaki, Dark confinement-deconfinement phase transition: A roadmap from Polyakov loop models to gravitational waves, *J. High Energy Phys.* **09** (2021) 060.
- [64] M. Reichert, F. Sannino, Z.-W. Wang, and C. Zhang, Dark confinement and chiral phase transitions: Gravitational waves vs matter representations, *J. High Energy Phys.* **01** (2022) 003.
- [65] M. Reichert and Z.-W. Wang, Gravitational waves from dark composite dynamics, *EPJ Web Conf.* **274**, 08003 (2022).
- [66] R. D. Pisarski, Quark gluon plasma as a condensate of  $SU(3)$  Wilson lines, *Phys. Rev. D* **62**, 111501 (2000).
- [67] R. D. Pisarski, Tests of the Polyakov loops model, *Nucl. Phys.* **A702**, 151 (2002).
- [68] R. D. Pisarski, Notes on the deconfining phase transition, in *Cargèse Summer School on QCD Perspectives on Hot and Dense Matter* (Springer Dordrecht, Dordrecht, Netherlands, 2002), pp. 353–384, [arXiv:hep-ph/0203271](#).
- [69] F. Sannino, Polyakov loops versus hadronic states, *Phys. Rev. D* **66**, 034013 (2002).
- [70] C. Ratti, M. A. Thaler, and W. Weise, Phases of QCD: Lattice thermodynamics and a field theoretical model, *Phys. Rev. D* **73**, 014019 (2006).
- [71] K. Fukushima and C. Sasaki, The phase diagram of nuclear and quark matter at high baryon density, *Prog. Part. Nucl. Phys.* **72**, 99 (2013).
- [72] K. Fukushima and V. Skokov, Polyakov loop modeling for hot QCD, *Prog. Part. Nucl. Phys.* **96**, 154 (2017).
- [73] P. M. Lo, B. Friman, O. Kaczmarek, K. Redlich, and C. Sasaki, Polyakov loop fluctuations in  $SU(3)$  lattice gauge theory and an effective gluon potential, *Phys. Rev. D* **88**, 074502 (2013).
- [74] H. Hansen, R. Stiele, and P. Costa, Quark and Polyakov-loop correlations in effective models at zero and non-vanishing density, *Phys. Rev. D* **101**, 094001 (2020).
- [75] P. N. Meisinger, T. R. Miller, and M. C. Ogilvie, Phenomenological equations of state for the quark gluon plasma, *Phys. Rev. D* **65**, 034009 (2002).
- [76] A. Dumitru, Y. Guo, Y. Hidaka, C. P. K. Altes, and R. D. Pisarski, How wide is the transition to deconfinement?, *Phys. Rev. D* **83**, 034022 (2011).
- [77] A. Dumitru, Y. Guo, Y. Hidaka, C. P. K. Altes, and R. D. Pisarski, Effective matrix model for deconfinement in pure gauge theories, *Phys. Rev. D* **86**, 105017 (2012).
- [78] K.-I. Kondo, Confinement–deconfinement phase transition and gauge-invariant gluonic mass in Yang-Mills theory, [arXiv:1508.02656](#).
- [79] R. D. Pisarski and V. V. Skokov, Chiral matrix model of the semi-QGP in QCD, *Phys. Rev. D* **94**, 034015 (2016).
- [80] H. Nishimura, R. D. Pisarski, and V. V. Skokov, Finite-temperature phase transitions of third and higher order in gauge theories at large  $N$ , *Phys. Rev. D* **97**, 036014 (2018).
- [81] Y. Guo and Q. Du, Two-loop perturbative corrections to the constrained effective potential in thermal QCD, *J. High Energy Phys.* **05** (2019) 042.
- [82] C. P. Korthals Altes, H. Nishimura, R. D. Pisarski, and V. V. Skokov, Free energy of a holonomous plasma, *Phys. Rev. D* **101**, 094025 (2020).
- [83] Y. Hidaka and R. D. Pisarski, Effective models of a semi-quark-gluon plasma, *Phys. Rev. D* **104**, 074036 (2021).
- [84] B. Lucini, M. Teper, and U. Wenger, The deconfinement transition in  $SU(N)$  gauge theories, *Phys. Lett. B* **545**, 197 (2002).
- [85] B. Lucini, M. Teper, and U. Wenger, The high temperature phase transition in  $SU(N)$  gauge theories, *J. High Energy Phys.* **01** (2004) 061.
- [86] B. Lucini, M. Teper, and U. Wenger, Properties of the deconfining phase transition in  $SU(N)$  gauge theories, *J. High Energy Phys.* **02** (2005) 033.
- [87] M. Panero, Thermodynamics of the QCD plasma and the large- $N$  limit, *Phys. Rev. Lett.* **103**, 232001 (2009).
- [88] S. Datta and S. Gupta, Continuum thermodynamics of the  $SU(N_c)$  gluon plasma, *Phys. Rev. D* **82**, 114505 (2010).
- [89] B. Lucini, A. Rago, and E. Rinaldi,  $SU(N_c)$  gauge theories at deconfinement, *Phys. Lett. B* **712**, 279 (2012).
- [90] K. Holland, M. Pepe, and U. J. Wiese, The deconfinement phase transition of  $Sp(2)$  and  $Sp(3)$  Yang-Mills theories in  $(2+1)$ -dimensions and  $(3+1)$ -dimensions, *Nucl. Phys.* **B694**, 35 (2004).
- [91] M. Pepe, Confinement and the center of the gauge group, *Proc. Sci. LAT2005* (2006) 017 [[arXiv:hep-lat/0510013](#)].
- [92] M. Pepe and U. J. Wiese, Exceptional deconfinement in  $G(2)$  gauge theory, *Nucl. Phys.* **B768**, 21 (2007).
- [93] G. Cossu, M. D’Elia, A. Di Giacomo, B. Lucini, and C. Pica,  $G(2)$  gauge theory at finite temperature, *J. High Energy Phys.* **10** (2007) 100.
- [94] M. Bruno, M. Caselle, M. Panero, and R. Pellegrini, Exceptional thermodynamics: The equation of state of  $G_2$  gauge theory, *J. High Energy Phys.* **03** (2015) 057.
- [95] T. Appelquist *et al.*, Stealth dark matter: Dark scalar baryons through the Higgs portal, *Phys. Rev. D* **92**, 075030 (2015).
- [96] T. Appelquist *et al.*, Detecting stealth dark matter directly through electromagnetic polarizability, *Phys. Rev. Lett.* **115**, 171803 (2015).
- [97] R. C. Brower *et al.* (Lattice Strong Dynamics Collaboration), Stealth dark matter confinement transition and gravitational waves, *Phys. Rev. D* **103**, 014505 (2021).
- [98] A. Maas and F. Zierler, Strong isospin breaking in  $Sp(4)$  gauge theory, *Proc. Sci. LATTICE2021* (2022) 130 [[arXiv:2109.14377](#)].
- [99] F. Zierler and A. Maas,  $Sp(4)$  SIMP dark matter on the lattice, *Proc. Sci. LHCP2021* (2021) 162.
- [100] S. Kulkarni, A. Maas, S. Mee, M. Nikolic, J. Pradler, and F. Zierler, Low-energy effective description of dark  $Sp(4)$  theories, *SciPost Phys.* **14**, 044 (2023).
- [101] J. M. Maldacena, The large  $N$  limit of superconformal field theories and supergravity, *Adv. Theor. Math. Phys.* **2**, 231 (1998).
- [102] S. S. Gubser, I. R. Klebanov, and A. M. Polyakov, Gauge theory correlators from noncritical string theory, *Phys. Lett. B* **428**, 105 (1998).
- [103] E. Witten, Anti-de Sitter space and holography, *Adv. Theor. Math. Phys.* **2**, 253 (1998).
- [104] O. Aharony, S. S. Gubser, J. M. Maldacena, H. Ooguri, and Y. Oz, Large  $N$  field theories, string theory and gravity, *Phys. Rep.* **323**, 183 (2000).



- [105] E. Witten, Anti-de Sitter space, thermal phase transition, and confinement in gauge theories, *Adv. Theor. Math. Phys.* **2**, 505 (1998).
- [106] I. R. Klebanov and M. J. Strassler, Supergravity and a confining gauge theory: Duality cascades and chi SB resolution of naked singularities, *J. High Energy Phys.* **08** (2000) 052.
- [107] J. M. Maldacena and C. Nunez, Towards the large  $N$  limit of pure  $N = 1$  superYang-Mills, *Phys. Rev. Lett.* **86**, 588 (2001).
- [108] A. H. Chamseddine and M. S. Volkov, NonAbelian BPS monopoles in  $N = 4$  gauged supergravity, *Phys. Rev. Lett.* **79**, 3343 (1997).
- [109] A. Butti, M. Grana, R. Minasian, M. Petrini, and A. Zaffaroni, The baryonic branch of Klebanov-Strassler solution: A supersymmetric family of SU(3) structure backgrounds, *J. High Energy Phys.* **03** (2005) 069.
- [110] R. C. Brower, S. D. Mathur, and C.-I. Tan, Glueball spectrum for QCD from AdS supergravity duality, *Nucl. Phys.* **B587**, 249 (2000).
- [111] A. Karch and E. Katz, Adding flavor to AdS/CFT, *J. High Energy Phys.* **06** (2002) 043.
- [112] M. Kruczenski, D. Mateos, R. C. Myers, and D. J. Winters, Meson spectroscopy in AdS/CFT with flavor, *J. High Energy Phys.* **07** (2003) 049.
- [113] T. Sakai and S. Sugimoto, Low energy hadron physics in holographic QCD, *Prog. Theor. Phys.* **113**, 843 (2005).
- [114] T. Sakai and S. Sugimoto, More on a holographic dual of QCD, *Prog. Theor. Phys.* **114**, 1083 (2005).
- [115] F. Bigazzi, A. Caddeo, A. L. Cotrone, and A. Paredes, Fate of false vacua in holographic first-order phase transitions, *J. High Energy Phys.* **12** (2020) 200.
- [116] F. R. Ares, M. Hindmarsh, C. Hoyos, and N. Jokela, Gravitational waves from a holographic phase transition, *J. High Energy Phys.* **04** (2021) 100.
- [117] Y. Bea, J. Casalderrey-Solana, T. Giannakopoulos, D. Mateos, M. Sanchez-Garitaonandia, and M. Zilhão, Bubble wall velocity from holography, *Phys. Rev. D* **104**, L121903 (2021).
- [118] F. Bigazzi, A. Caddeo, T. Canneli, and A. L. Cotrone, Bubble wall velocity at strong coupling, *J. High Energy Phys.* **08** (2021) 090.
- [119] O. Henriksson, Black brane evaporation through D-brane bubble nucleation, *Phys. Rev. D* **105**, L041901 (2022).
- [120] F. R. Ares, O. Henriksson, M. Hindmarsh, C. Hoyos, and N. Jokela, Effective actions and bubble nucleation from holography, *Phys. Rev. D* **105**, 066020 (2022).
- [121] F. R. Ares, O. Henriksson, M. Hindmarsh, C. Hoyos, and N. Jokela, Gravitational waves at strong coupling from an effective action, *Phys. Rev. Lett.* **128**, 131101 (2022).
- [122] E. Morgante, N. Ramberg, and P. Schwaller, Gravitational waves from dark SU(3) Yang-Mills theory, *Phys. Rev. D* **107**, 036010 (2023).
- [123] S. Borsanyi, R. Kara, Z. Fodor, D. A. Godzieba, P. Parotto, and D. Sexty, Precision study of the continuum SU(3) Yang-Mills theory: How to use parallel tempering to improve on supercritical slowing down for first order phase transitions, *Phys. Rev. D* **105**, 074513 (2022).
- [124] B. Svetitsky and L. G. Yaffe, Critical behavior at finite temperature confinement transitions, *Nucl. Phys.* **B210**, 423 (1982).
- [125] L. G. Yaffe and B. Svetitsky, First order phase transition in the SU(3) gauge theory at finite temperature, *Phys. Rev. D* **26**, 963 (1982).
- [126] H. Saito, S. Ejiri, S. Aoki, T. Hatsuda, K. Kanaya, Y. Maezawa, H. Ohno, and T. Umeda (WHOT-QCD Collaboration), Phase structure of finite temperature QCD in the heavy quark region, *Phys. Rev. D* **84**, 054502 (2011); **85**, 079902(E) (2012).
- [127] S. Ejiri, S. Itagaki, R. Iwami, K. Kanaya, M. Kitazawa, A. Kiyohara, M. Shirogane, and T. Umeda (WHOT-QCD Collaboration), End point of the first-order phase transition of QCD in the heavy quark region by reweighting from quenched QCD, *Phys. Rev. D* **101**, 054505 (2020).
- [128] A. Kiyohara, M. Kitazawa, S. Ejiri, and K. Kanaya, Finite-size scaling around the critical point in the heavy quark region of QCD, *Phys. Rev. D* **104**, 114509 (2021).
- [129] M. Fromm, J. Langelage, S. Lottini, and O. Philipsen, The QCD deconfinement transition for heavy quarks and all baryon chemical potentials, *J. High Energy Phys.* **01** (2012) 042.
- [130] F. Cuteri, O. Philipsen, A. Schön, and A. Sciarra, Deconfinement critical point of lattice QCD with  $N_f = 2$  Wilson fermions, *Phys. Rev. D* **103**, 014513 (2021).
- [131] S. Borsanyi, Z. Fodor, J. N. Guenther, R. Kara, P. Parotto, A. Pasztor, and D. Sexty, The upper right corner of the Columbia plot with staggered fermions, *Proc. Sci. LATTICE2021* (2022) 496 [arXiv:2112.04192].
- [132] G. Aarts *et al.*, Phase transitions in particle physics—results and perspectives from lattice quantum chromodynamics, *Prog. Part. Nucl. Phys.* **133**, 104070 (2023).
- [133] K. Kajantie, C. Montonen, and E. Pietarinen, Phase transition of SU(3) gauge theory at finite temperature, *Z. Phys. C* **9**, 253 (1981).
- [134] T. Celik, J. Engels, and H. Satz, The order of the deconfinement transition in SU(3) Yang-Mills theory, *Phys. Lett.* **125B**, 411 (1983).
- [135] J. B. Kogut, H. Matsuoka, M. Stone, H. W. Wyld, S. H. Shenker, J. Shigemitsu, and D. K. Sinclair, Quark and gluon latent heats at the deconfinement phase transition in SU(3) gauge theory, *Phys. Rev. Lett.* **51**, 869 (1983).
- [136] B. Svetitsky and F. Fucito, Latent heat of the SU(3) gauge theory, *Phys. Lett.* **131B**, 165 (1983).
- [137] S. A. Gottlieb, J. Kuti, D. Toussaint, A. D. Kennedy, S. Meyer, B. J. Pendleton, and R. L. Sugar, The deconfining phase transition and the continuum limit of lattice quantum chromodynamics, *Phys. Rev. Lett.* **55**, 1958 (1985).
- [138] F. R. Brown, N. H. Christ, Y. F. Deng, M. S. Gao, and T. J. Woch, Nature of the deconfining phase transition in SU(3) lattice gauge theory, *Phys. Rev. Lett.* **61**, 2058 (1988).
- [139] M. Fukugita, M. Okawa, and A. Ukawa, Order of the deconfining phase transition in SU(3) lattice gauge theory, *Phys. Rev. Lett.* **63**, 1768 (1989).
- [140] P. Bacilieri *et al.*, A new computation of the correlation length near the deconfining transition in SU(3), *Phys. Lett. B* **224**, 333 (1989).



- [141] N. A. Alves, B. A. Berg, and S. Sanielevici, Binder energy cumulant for SU(3) lattice gauge theory, *Phys. Lett. B* **241**, 557 (1990).
- [142] G. Boyd, J. Engels, F. Karsch, E. Laermann, C. Legeland, M. Lutgemeier, and B. Petersson, Equation of state for the SU(3) gauge theory, *Phys. Rev. Lett.* **75**, 4169 (1995).
- [143] G. Boyd, J. Engels, F. Karsch, E. Laermann, C. Legeland, M. Lutgemeier, and B. Petersson, Thermodynamics of SU(3) lattice gauge theory, *Nucl. Phys.* **B469**, 419 (1996).
- [144] S. Borsanyi, G. Endrodi, Z. Fodor, S. D. Katz, and K. K. Szabo, Precision SU(3) lattice thermodynamics for a large temperature range, *J. High Energy Phys.* **07** (2012) 056.
- [145] M. Shirogane, S. Ejiri, R. Iwami, K. Kanaya, and M. Kitazawa, Latent heat at the first order phase transition point of SU(3) gauge theory, *Phys. Rev. D* **94**, 014506 (2016).
- [146] E. Bennett, D. K. Hong, J.-W. Lee, C. J. D. Lin, B. Lucini, M. Piai, and D. VDACCHINO, Sp(4) gauge theory on the lattice: Towards SU(4)/Sp(4) composite Higgs (and beyond), *J. High Energy Phys.* **03** (2018) 185.
- [147] E. Bennett, D. K. Hong, J.-W. Lee, C. J. D. Lin, B. Lucini, M. Piai, and D. VDACCHINO, Sp(4) gauge theories on the lattice:  $N_f = 2$  dynamical fundamental fermions, *J. High Energy Phys.* **12** (2019) 053.
- [148] E. Bennett, D. K. Hong, J.-W. Lee, C.-J. D. Lin, B. Lucini, M. Mesiti, M. Piai, J. Rantaharju, and D. VDACCHINO, Sp(4) gauge theories on the lattice: Quenched fundamental and antisymmetric fermions, *Phys. Rev. D* **101**, 074516 (2020).
- [149] E. Bennett, J. Holligan, D. K. Hong, J.-W. Lee, C. J. D. Lin, B. Lucini, M. Piai, and D. VDACCHINO, Color dependence of tensor and scalar glueball masses in Yang-Mills theories, *Phys. Rev. D* **102**, 011501 (2020).
- [150] E. Bennett, J. Holligan, D. K. Hong, J.-W. Lee, C. J. D. Lin, B. Lucini, M. Piai, and D. VDACCHINO, Glueballs and strings in Sp(2N) Yang-Mills theories, *Phys. Rev. D* **103**, 054509 (2021).
- [151] E. Bennett, D. K. Hong, H. Hsiao, J.-W. Lee, C. J. D. Lin, B. Lucini, M. Mesiti, M. Piai, and D. VDACCHINO, Lattice studies of the Sp(4) gauge theory with two fundamental and three antisymmetric Dirac fermions, *Phys. Rev. D* **106**, 014501 (2022).
- [152] E. Bennett, D. K. Hong, J.-W. Lee, C. J. D. Lin, B. Lucini, M. Piai, and D. VDACCHINO, Sp(2N) Yang-Mills theories on the lattice: Scale setting and topology, *Phys. Rev. D* **106**, 094503 (2022).
- [153] E. Bennett, D. K. Hong, J.-W. Lee, C. J. D. Lin, B. Lucini, M. Piai, and D. VDACCHINO, Color dependence of the topological susceptibility in Yang-Mills theories, *Phys. Lett. B* **835**, 137504 (2022).
- [154] E. Bennett, J. Holligan, D. K. Hong, H. Hsiao, J.-W. Lee, C. J. D. Lin, B. Lucini, M. Mesiti, M. Piai, and D. VDACCHINO, Sp(2N) lattice gauge theories and extensions of the standard model of particle physics, *Universe* **9**, 236 (2023).
- [155] E. Bennett, H. Hsiao, J.-W. Lee, B. Lucini, A. Maas, M. Piai, and F. Zierler, Singlets in gauge theories with fundamental matter, [arXiv:2304.07191](https://arxiv.org/abs/2304.07191).
- [156] K. Langfeld, B. Lucini, and A. Rago, The density of states in gauge theories, *Phys. Rev. Lett.* **109**, 111601 (2012).
- [157] K. Langfeld and J. M. Pawłowski, Two-color QCD with heavy quarks at finite densities, *Phys. Rev. D* **88**, 071502 (2013).
- [158] K. Langfeld, B. Lucini, R. Pellegrini, and A. Rago, An efficient algorithm for numerical computations of continuous densities of states, *Eur. Phys. J. C* **76**, 306 (2016).
- [159] G. Cossu, D. Lancaster, B. Lucini, R. Pellegrini, and A. Rago, Ergodic sampling of the topological charge using the density of states, *Eur. Phys. J. C* **81**, 375 (2021).
- [160] F. Springer and D. Schaich, Density of states for gravitational waves, *Proc. Sci. LATTICE2021* (2022) 043 [[arXiv:2112.11868](https://arxiv.org/abs/2112.11868)].
- [161] F. Springer and D. Schaich, Progress applying density of states for gravitational waves, *EPJ Web Conf.* **274**, 08008 (2022).
- [162] F. Springer and D. Schaich (Lattice Strong Dynamics (LSD) Collaboration), Advances in using density of states for large-N Yang-Mills, *Proc. Sci. LATTICE2022* (2023) 223.
- [163] D. Mason, B. Lucini, M. Piai, E. Rinaldi, and D. VDACCHINO, The density of states method in Yang-Mills theories and first order phase transitions, *EPJ Web Conf.* **274**, 08007 (2022).
- [164] D. Mason, B. Lucini, M. Piai, E. Rinaldi, and D. VDACCHINO, The density of state method for first-order phase transitions in Yang-Mills theories, *Proc. Sci. LATTICE2022* (2023) 216 [[arXiv:2212.01074](https://arxiv.org/abs/2212.01074)].
- [165] B. Lucini, W. Fall, and K. Langfeld, Overcoming strong metastabilities with the LLR method, *Proc. Sci. LATTICE2016* (2016) 275 [[arXiv:1611.00019](https://arxiv.org/abs/1611.00019)].
- [166] H. Robbins and S. Monro, A stochastic approximation method, *Ann. Math. Stat.* **22**, 400 (1951).
- [167] F. Karsch, SU(N) gauge theory couplings on asymmetric lattices, *Nucl. Phys.* **B205**, 285 (1982).
- [168] B. Lucini, D. Mason, M. Piai, E. Rinaldi, and D. VDACCHINO, First-order phase transitions in Yang-Mills theories and the density of state method—data and analysis code release (2023), [10.5281/zenodo.8124749](https://doi.org/10.5281/zenodo.8124749).
- [169] B. Lucini, D. Mason, M. Piai, E. Rinaldi, and D. VDACCHINO, First-order phase transitions in Yang-Mills theories and the density of state method—HiRep LLR code v1.0.0 (2023), [10.5281/zenodo.8134756](https://doi.org/10.5281/zenodo.8134756).
- [170] [www.dirac.ac.uk](http://www.dirac.ac.uk).
- [171] M. Creutz, Monte Carlo study of quantized SU(2) gauge theory, *Phys. Rev. D* **21**, 2308 (1980).
- [172] N. Cabibbo and E. Marinari, A new method for updating SU(N) matrices in computer simulations of gauge theories, *Phys. Lett.* **119B**, 387 (1982).